Human Molecular Genetics, 2022, Vol. 31, 11, 1884–1908
https://doi.org/10.1093/hmg/ddac028
Advance access publication date 31 January 2022
Original Article

Deregulation of microtubule organization and RNA metabolism in *Arx* models for lissencephaly and developmental epileptic encephalopathy

Denise Drongitis[1,†], Marianna Caterino[2,3,†], Lucia Verrillo[1], Pamela Santonicola[4], Michele Costanzo[2,3], Loredana Poeta[1,5], Benedetta Attianese[1], Adriano Barra[1], Gaetano Terrone[6], Maria Brigida Lioi[5], Simona Paladino[2], Elia Di Schiavi[4], Valerio Costa[1], Margherita Ruoppolo[2,3] and Maria Giuseppina Miano[1,*]

[1]Institute of Genetics and Biophysics "Adriano Buzzati-Traverso", National Research Council of Italy, 80131, Naples, Italy
[2]Department of Molecular Medicine and Medical Biotechnology, University of Naples "Federico II", 80131 Naples, Italy
[3]CEINGE - Biotecnologie Avanzate s.c.a.r.l., 80145 Naples, Italy
[4]Institute of Biosciences and BioResources, National Research Council of Italy, 80131, Naples, Italy
[5]Department of Science, University of Basilicata, 85100 Potenza, Italy
[6]Department of Translational Medicine, Child Neurology Unit, University of Naples "Federico II", 80131 Naples, Italy
*To whom correspondence should be addressed at: Institute of Genetics and Biophysics "Adriano Buzzati-Traverso", CNR Via Pietro Castellino, 111, 80131 Naples, Italy. Tel: +390816132261; Fax: +39081613706; Email: mariag.miano@igb.cnr.it

[†]These authors equally contributed to this work.

Abstract

X-linked lissencephaly with abnormal genitalia (XLAG) and developmental epileptic encephalopathy-1 (DEE1) are caused by mutations in the Aristaless-related homeobox (*ARX*) gene, which encodes a transcription factor responsible for brain development. It has been unknown whether the phenotypically diverse XLAG and DEE1 phenotypes may converge on shared pathways. To address this question, a label-free quantitative proteomic approach was applied to the neonatal brain of *Arx* knockout ($Arx^{KO/Y}$) and knock-in polyalanine ($Arx^{(GCG)7/Y}$) mice that are respectively models for XLAG and DEE1. Gene ontology and protein–protein interaction analysis revealed that cytoskeleton, protein synthesis and splicing control are deregulated in an allelic-dependent manner. Decreased α-tubulin content was observed both in *Arx* mice and *Arx/alr-1*(*KO*) *Caenorhabditis elegans* ,and a disorganized neurite network in murine primary neurons was consistent with an allelic-dependent secondary tubulinopathy. As distinct features of $Arx^{(GCG)7/Y}$ mice, we detected eIF4A2 overexpression and translational suppression in cortex and primary neurons. Allelic-dependent differences were also established in alternative splicing (AS) regulated by PUF60 and SAM68. Abnormal AS repertoires in *Neurexin-1*, a gene encoding multiple pre-synaptic organizers implicated in synaptic remodelling, were detected in *Arx/alr-1*(*KO*) animals and in $Arx^{(GCG)7/Y}$ epileptogenic brain areas and depolarized cortical neurons. Consistent with a conserved role of ARX in modulating AS, we propose that the allelic-dependent secondary synaptopathy results from an aberrant Neurexin-1 repertoire. Overall, our data reveal alterations mirroring the overlapping and variant effects caused by null and polyalanine expanded mutations in *ARX*. The identification of these effects can aid in the design of pathway-guided therapy for *ARX* endophenotypes and NDDs with overlapping comorbidities.

Received: October 30, 2021. **Revised:** January 10, 2022. **Accepted:** January 26, 2022

Graphical Abstract

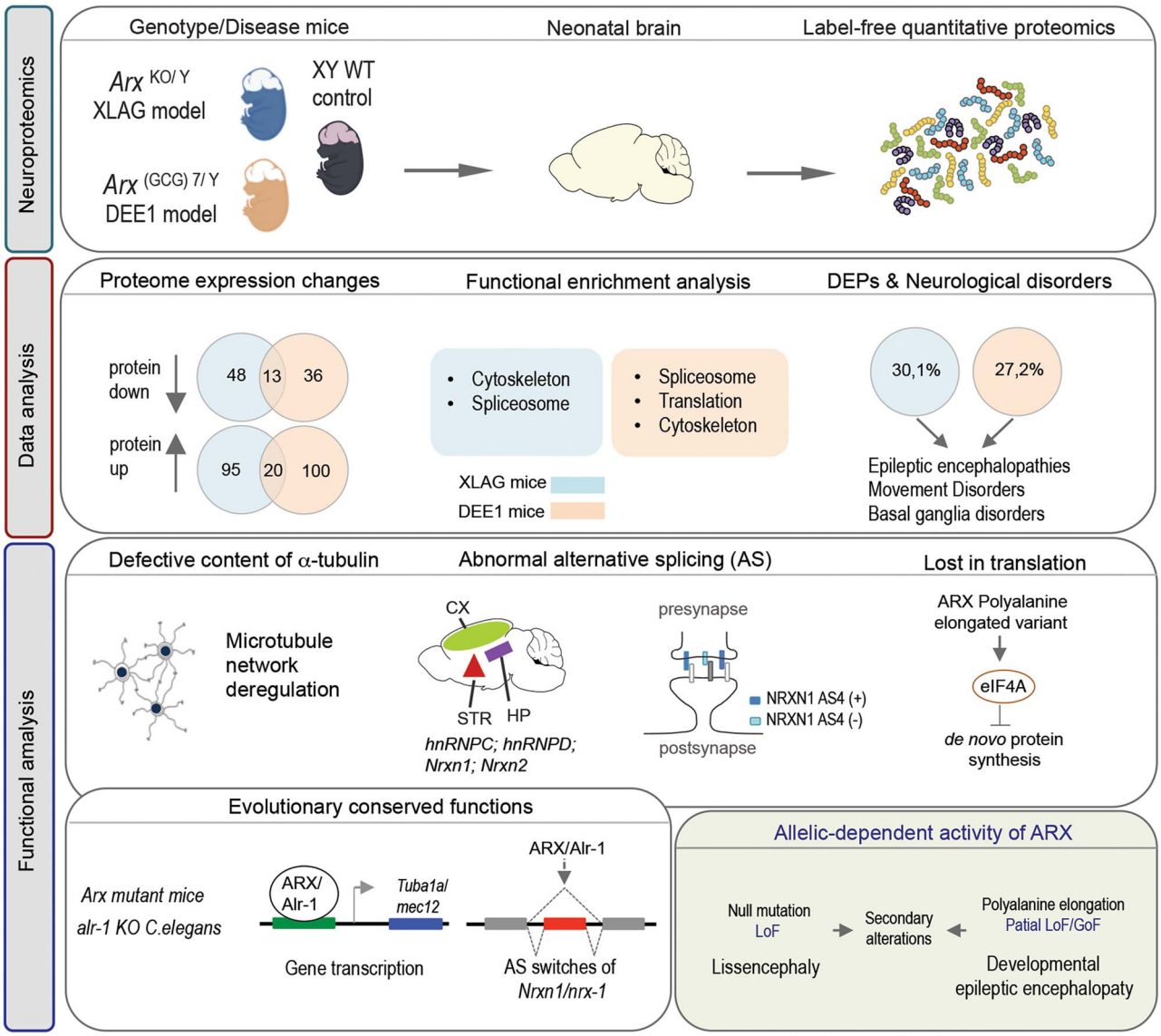

Introduction

The correct development of the mammalian brain requires fine-tuned orchestration of several homeotic transcription factors (TFs), in which deregulation may cause neurodevelopmental diseases (NDDs) (1). Aristaless-related homeobox (ARX; MIM 300382) is an X-chromosome gene that encodes a bifunctional TF absolutely required for proper brain morphogenesis. Mutations in *ARX* have been found in a wide range of incurable NDDs affecting male children, with severity dependent on the type of alteration (2–4). Point missense mutations affecting the homeobox domain (HD) in *ARX* lead to loss of function (LoF) causing X-linked lissencephaly with agenesis of the corpus callosum and ambiguous genitalia (XLAG; MIM 300215). In addition to profound structural brain anomalies, XLAG patients have early-onset intractable seizures, and severe psychomotor retardation, often dying within the first months of life (5–7). In contrast, partial LoF alterations by elongations of the first polyalanine (polyAla) tract in the protein cause developmental and epileptic encephalopathy 1 (DEE1; MIM 308350; also named early infantile epileptic encephalopathy 1), a less severe disease compared to XLAG (2,3,7–10). DEE1 patients rather develop pharmaco-resistant paediatric epilepsy characterized by tonic spasms, arrest of psychomotor development, hand dystonia and severe intellectual disability (ID) but with an apparently normal brain structure (11). Previous studies conducted by us and others have shown that XLAG mutations disrupt the transcriptional program controlled by ARX; whereas, expansions of the polyAla tracts are hypomorphic mutations, with reduced transcriptional activity and

binding properties (3,4,10,12,13). This partially faulty activity of the elongated ARX protein is associated with the aggregation of mutant proteins, a phenomenon also detected in other instances of pathogenic expanded repeats that might add a possible gain of function (GoF) increasing the phenotype severity (3,14,15).

These findings support the hypothesis that differences in the clinical manifestations of XLAG and DEE1 may correlate with a varying degree of ARX function: the complete loss of transcriptional activity exhibited by LoF mutations produces the severe cortical malformation whereas the partial impairment of transcriptional activity with a potential GoF activity shown by polyAla elongations (partial LoF/GoF) induce the refractory epilepsy (16). Whether, where and when the functional features of polyAla elongations synergize each other and how they impact disease heterogeneity are completely unknown. However, the identification of the molecular basis of $Arx^{(GCG)7/Y}$ pathophysiology remains a big task of ARX studies whose investigation could be fundamental in the identification of relevant therapeutics.

A considerable advance in the analysis of XLAG and DEE1 pathogenesis was afforded by the generation of two *Arx* transgenic mice: the knockout $Arx^{KO/Y}$, which harbours a null mutation that abolishes the TF activity of ARX and recapitulates several XLAG signs including a small brain, defective neuronal migration and neonatal death (Table 1) (17), and the knock-in $Arx^{(GCG)7/Y}$ (also referred as *Arx* polyalanine), harbouring a trinucleotide repeat mutation that expands the first polyAla tract and thus impairs but does not abolish ARX activity. These mice exhibit an apparently normal brain structure but develop severe seizures in young animals (at postnatal days 35 or 40) in a phenotype resembling DEE1 (Table 1) (6,18,19). In ongoing efforts to understand the function of ARX in health and disease conditions, transcriptomic analyses were carried out in embryonic brains of *Arx* transgenic mice (12,20–22). These studies have shown the crucial role of the cell–cell adhesion pathway and synaptic transmission at the early stage of embryonic development (12,20–22). Very importantly, ARX plays multiple and distinct cell-autonomous roles during corticogenesis in the regulation of cell cycle of neuronal progenitor cells, morphology and radial migration of pyramidal neurons and tangential migration of interneurons (16). Besides, it regulates dorso-ventral identity in the forebrain patterning and growth (23). It is noteworthy that very few pathway biomarkers of the disease at birth have been reported making it difficult to explain at molecular level the basis of XLAG and DEE1—both in patients and mouse models—associated with alterations in ARX with LoF (caused by null mutation) and partial LoF/GoF (caused by polyAla elongation) activities.

Extending further, we have performed for the first time a comprehensive analysis by mass spectrometry (MS)-based label-free quantitative proteomics of neonatal brains of the XLAG-*Arx* mice ($Arx^{KO/Y}$) and the DEE1-*Arx* mice ($Arx^{(GCG)7/Y}$). Computational examination of the results reveals both overlaps and genotype-dependent differences between the two allelic conditions. Integration with publicly available *Arx* datasets (RNA-Seq transcriptome and ChIP-on-chip data) implicates several differentially expressed proteins (DEPs) in the neurological disorders. Further functional analysis focusing on top hits validated deregulated molecular pathways in both *Arx* mutant mice. Furthermore, taking advantage of the evolutionary conserved ARX activity between mammals and nematodes (4), we extended our analysis to the *C. elegans alr-1*(*KO*) mutant, ablated for the orthologue of *Arx,* that shows axon guidance and dendritic defects, touch insensitivity and faulty GABAergic maturation (4,24). Altogether, these findings highlight the pleiotropic consequences of LoF and partial LoF/GoF activities of *Arx* mutations thus identifying secondary alterations that differentially affect XLAG- and DEE1-*Arx* brain pups.

Results

Quantitative proteomics uncovers both profound similarities and exclusive features in neonatal brains of $Arx^{KO/Y}$ and $Arx^{(GCG)7/Y}$ mice

The alterations in neonatal brain expression profiles associated with the null mutation in $Arx^{KO/Y}$ and the elongated polyalanine mutation $(GCG)_7$ in $Arx^{(GCG)7/Y}$ were quantitatively determined by label-free quantitative proteomics. Both brain proteomes of $Arx^{KO/Y}$ and $Arx^{(GCG)7/Y}$ pups were compared with XY wild-type (WT) ones. In particular, comparative analysis was performed using five males from each genotype and four matched XY WT mice. Thus, liquid chromatography–tandem mass spectrometry (LC–MS/MS) analysis produced two distinct proteomic datasets, $Arx^{KO/Y}$ and $Arx^{(GCG)7/Y}$, including 176 and 169 DEPs respectively (Supplementary Material, Tables S1 and S2). The DEPs are graphically represented in volcano plots (Fig. 1A) highlighting interesting proteins that are discussed here. The NSAF protein abundances were able to discriminate between the compared groups for both conditions (Supplementary Material, Fig. S1). Furthermore, the regulated proteomes of the two different genotypes were intersected in order to select common and exclusive features (Fig. 1B). Accordingly, 48 proteins were downregulated in $Arx^{KO/Y}$ datasets and 36 in $Arx^{(GCG)7/Y}$, exclusively; 13 proteins were commonly down-regulated in $Arx^{KO/Y}$ and $Arx^{(GCG)7/Y}$. Conversely, 95 proteins were upregulated in $Arx^{KO/Y}$ datasets and 100 in $Arx^{(GCG)7/Y}$, exclusively; 20 proteins were commonly upregulated in $Arx^{KO/Y}$ and $Arx^{(GCG)7/Y}$.

Top dysregulated canonical pathways and GO terms in $Arx^{KO/Y}$ and $Arx^{(GCG)7/Y}$

The lists of significant DEPs in the whole brains of $Arx^{KO/Y}$ and $Arx^{(GCG)7/Y}$ were clustered according to their gene ontology (GO) categories, using DAVID. The most interesting altered GO biological process, cellular component and molecular function were reported in

Table 1. Summary of the key features of *Arx*-disease models used in LC–MS/MS study

Name	Mutation	Viability	Brain abnormalities	Epilepsy	Human disease	References
$Arx^{KO/Y}$	Deletion of exons 1 and 2 of *Arx* gene	Perinatal death (at postnatal day 1 or 2)	Impaired radial and tangential migration of ventral forebrain neurons; Structural abnormalities in the striatum and pallidum; Decrease in cholinergic interneurons of the striatum and basal telencephalon.	No data	XLAG	(17,18,99)
$Arx^{(GCG)7/Y}$	Seven GCG triplets inserted in polyalanine tract 1 of exon 2	Up to 5 months	No gross malformations; Impaired tangential migration of interneurons to the striatum; Loss of cholinergic, striatal and ventral forebrain interneurons.	Spontaneous tonic–clonic seizures (at P30); Sudden death during epileptic attack	DEE1	(19)

Figure 1C (Supplementary Material, Tables S3 and S4). Based on the most significantly enriched IPA canonical pathways (*P*-value < 1.0E-03), 12 top-ranked terms were related to cytoskeleton, migration and neuronal plasticity in $Arx^{KO/Y}$ (Fig 1C; Supplementary Material, Table S5). Among them, the most significant term results in the remodelling of the epithelial adherens junctions pathway (*P*-value 9.30E-11), whose main role is to preserve cortical architecture and buffer the mechanical forces exerted by the cortical expansion (25).

In contrast, differential $Arx^{(GCG)7/Y}$ proteome clustered into 10 pathways (*P*-value < 1.0E-03) (Fig. 1C; Supplementary Material, Table S6) including eukaryotic translation initiation factor-2 (*eIF2*) signalling (*P*-value 1.4E-22; Supplementary Material, Table S6), regulation of *eIF4* and *p70S6K* (*P*-value 8.31E-08), *mTOR* signalling (*P*-value 3.56E-06), protein ubiquitination (*P*-value 1.15E-07) and actin cytoskeleton signalling (*P*-value 7.85E-05). In addition, splicing of mRNA (*P*-value 4.26E-11) and processing of RNA (*P*-value 5.82E-11) were highlighted as significant molecular functions (Supplementary Material, Table S6) in the $Arx^{(GCG)7/Y}$ neonatal brain. These results directly indicate new functions controlled by ARX as protein formation and metabolism, as well as cytoskeleton signalling, are possibly related to the gradual process by which the $Arx^{(GCG)7/Y}$ brain develops seizures. We were surprised to not find specific alterations in the development and functioning of GABAergic neurons or cholinergic neurons that—as previously described—are affected in *Arx* mutant mice (26–28). Probably due to the analytical sensitivity of untargeted proteomic analysis performed on the whole brain of the *Arx* mutant mice, we were not able to detect defects affecting a specific brain region or small neuronal populations. Very interestingly, cross-matching the IPA annotation disease tool and OMIM database revealed that 30.1% of DEPs in $Arx^{KO/Y}$ and 27.2% of DEPs in $Arx^{(GCG)7/Y}$ datasets are associated with multiple neurological disorders, including epileptic encephalopathies (EEs), basal ganglia diseases (BGDs) and movement disorders (MDs), all of which present comorbidities overlapping with *ARX* comorbidities and phenotypes (Supplementary Material, Fig. S2 and Table S7) (29,30). Related to BGDs and MDs, *ARX* expression is known to be present in neurons of the basal ganglia, a brain area involved in sensorimotor processing and control of precision gripping (29).

Functional enrichment analysis of $Arx^{KO/Y}$ and $Arx^{(GCG)7/Y}$ neonatal brain proteins identified shared and distinct disease-related pathways

The STRING PPI network analysis of the differential $Arx^{KO/Y}$ dataset generated microtubule cytoskeleton (GO_CC:0015630), actin cytoskeleton (GO_CC:0015629) and spliceosome (KEGG:mmu03040) (Fig. 2A) as the main clusters. The relative abundance values of proteins involved in these hits are represented in the heat maps (Fig. 2B). In particular, DEPs as tubulin alpha 1a and 4a (TUBA1A and TUBA4A), tubulin beta 2A class IIa and IIb (TUBB2A and TUBB2B), tubulin beta 3 Class III (TUBB3), tubulin beta 6 Class V (TUBB6), microtubule-associated protein RP/EB family member 1 (MAPRE1), actin-related protein 2/3 complex subunit 5 (ARPC5), actin-related protein 2/3 complex subunit 1A (ARPC1A) and the member RAS oncogene family 5A (RAB5A) are biomarkers for microtubule (MT) and actin–cytoskeleton regulation (Supplementary Material, Table S5 and Fig. S3A) (31–33). In addition, nine DEPs, including the splicing factors poly(U) binding splicing factor 60 (PUF60) and non-POU domain-containing octamer-binding protein (NONO), belong to the spliceosome (Supplementary Material, Table S5; Fig. 2B).

The STRING PPI network analysis of differential $Arx^{(GCG)7/Y}$ dataset revealed significant enrichment in proteasomes (KEGG:mmu03050), RNA binding (GO_MF:0003723)/spliceosomes (KEGG:mmu03040), translation (GO_BP:0006412)/ribosome (KEGG:mmu03010) and cytoskeleton (GO_CC:0005856)/intracellular transport (GO_BP:0046907) (Fig. 3A). The relative abundance values of

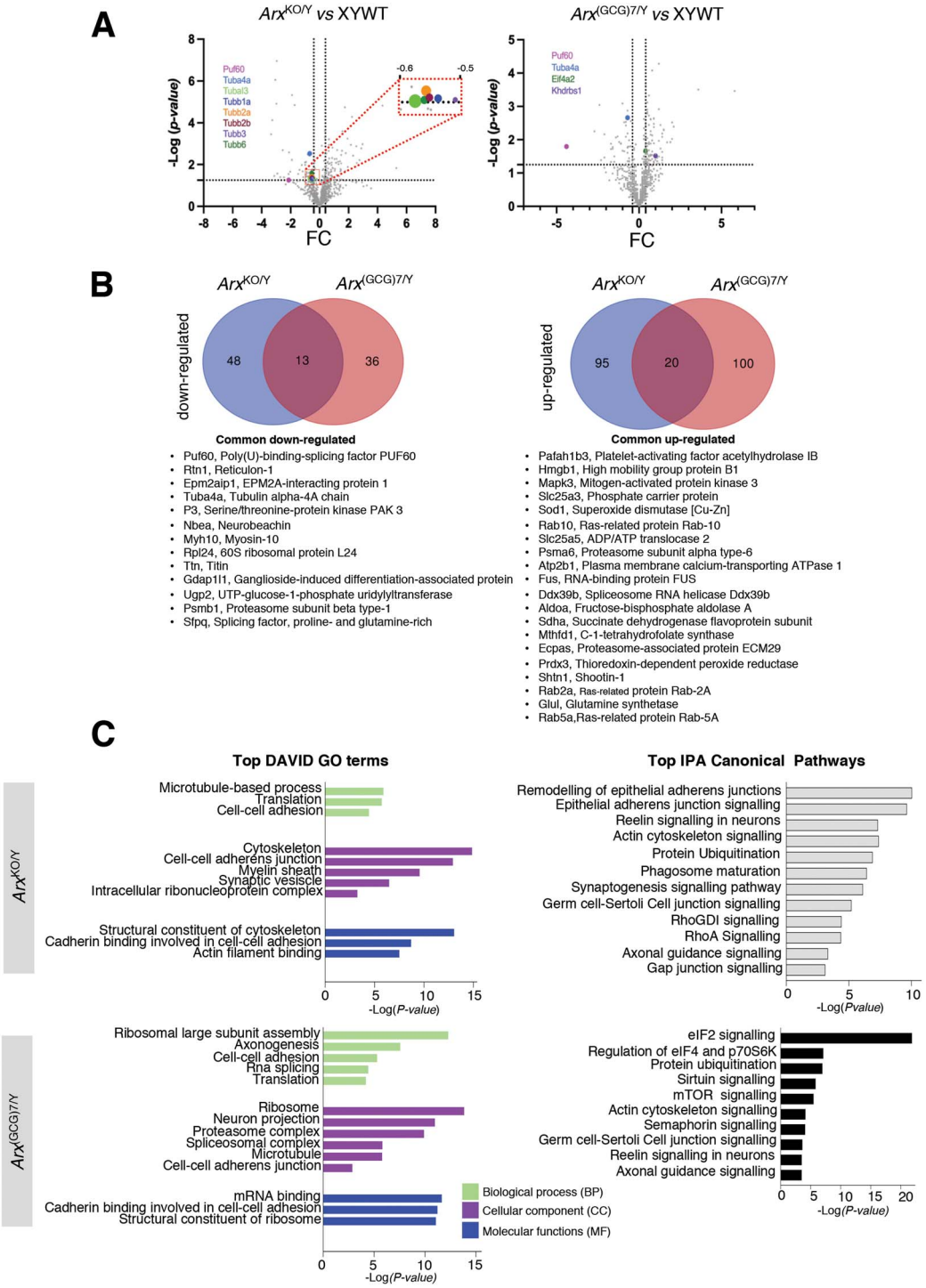

Figure 1. Comparative analysis of $Arx^{KO/Y}$ and $Arx^{(GCG)/Y}$ brain proteomes versus XY WT. (**A**) The differential protein expression profile in brain $Arx^{KO/Y}$ and $Arx^{(GCG)/Y}$ was obtained plotting $\log_2$ FC, reported on x-axis, against the statistical significance, reported as –log *P*-value on y-axis. FC and *P*-value were calculated using protein quantitative datasets obtained by five independent experiments for $Arx^{KO/Y}$ and $Arx^{(GCG)/Y}$ proteomes and four independent experiments for XY WT. Some selected DEPs are highlighted. (**B**) The Venn diagram reports common and exclusive deregulated proteins in $Arx^{KO/Y}$ and $Arx^{(GCG)/Y}$. The common downregulated and upregulated proteins are listed on the right of the figure. **(C)** Top IPA canonical pathways (left panels) and DAVID Gene ontology terms (right panels) are enriched for both whole neonatal brains of *Arx* $^{(KO)/Y}$ and $Arx^{(GCG)/Y}$. BP, biological processes; CC, cellular component and MF, molecular function.

proteins involved in these hits are represented in the heat maps (Fig. 3B). Interestingly, in $Arx^{(GCG)/7Y}$, 11 DEPs belong to the proteasome complex, including the regulatory particle and α - and β -subunits of 26S (Supplementary Material, Fig. S3B). Conversely, 17 DEPs, including the splicing factors PUF60 and KH RNA-binding domain containing, signal transduction-associated 1 (KHDRBS1; also named SAM68), belong to the spliceosomes (Fig. 3B; Supplementary Material, Table S2). Furthermore, 24 DEPs, including eukaryotic translation initiation factor

4A2 (eIF4A2), are involved in ribosomal activity and translation initiation (Fig. 3B; Supplementary Material, Fig. S3C) (34). Finally, 22 DEPs are involved in cytoskeleton organization/intracellular transport (Fig. 3B). The proteomic data suggest common alterations in pathways, such as cytoskeleton remodelling and spliceosomes, affecting both the analysed *Arx*-related genotypes, as a consequence of lost or impaired ARX activity. Of note, in $Arx^{(GCG)7/Y}$, there were exclusive alterations in proteasomes and translation/ribosomes that presumably result from the action of the *Arx* polyalanine-elongated protein.

$Arx^{KO/Y}$ and $Arx^{(GCG)7/Y}$ DEPs encoded by ARX-bound genes and expressed in the embryonic brain

As ARX is a central TF of mammalian brain development, we investigated which DEPs in $Arx^{KO/Y}$ and $Arx^{(GCG)7/Y}$ are encoded by potential ARX-target genes (35). Coupling publicly available data from chromatin immunoprecipitation followed by hybridization on mouse promoter arrays (ChIP-on-chip) and proteomic results, we identified nine and seven ARX-bound genes, whose encoded proteins are respectively DEPs in $Arx^{KO/Y}$ and $Arx^{(GCG)7/Y}$ (Fig. 4A; Supplementary Material, Table S8). Remarkably, among the nine proteins altered in $Arx^{KO/Y}$ mice (Fig. 4A; Supplementary Material, Table S8), three (i.e. TUBA1A; vesicle amine transport 1, VAT1; and vesicle transport through interaction with T-SNAREs 1B, VTI1B) are involved in cytoskeleton remodelling and synaptic vesicle activities (36–38). Similarly, in $Arx^{(GCG)7/Y}$, three (i.e. Profilin-2, PFN2; synaptic vesicle glycoprotein 2A, SV2A; and sodium/calcium exchanger 1, SLC8A1) are involved in cytoskeleton and vesicle trafficking (Supplementary Material, Table S8) (39–41). Moreover, a very intriguing ARX target is IF4A2 (alias of eIF4A2), an ATP-dependent RNA helicase in the eIF4 complex that has been identified as critically involved in other trinucleotide repeats disorders (34,42). Finally, RAB5A, involved in cytoskeleton and vesicle trafficking (32), and superoxide dismutase (SOD1), involved in superoxide radical metabolism (43,44), were identified as deregulated in both proteomic datasets (Supplementary Material, Table S8).

As the pathophysiology of XLAG and DEE1 begins early in embryogenesis, we analysed publicly available transcriptome data of E14.5 XY WT and E14.5 *Arx*-ablated cortices (GSE12956) (20,45) to detect DEPs encoded by early expressed genes (Supplementary Material, Fig. S4A). Relevant to $Arx^{KO/Y}$, we found that most of the genes in epithelial adherens junction signalling, cytoskeleton remodelling, synaptogenesis and axonal guidance signalling were expressed early in embryogenesis, including the ARX target genes *Tuba1a*, *Rab5a* and *Vit1b*. Moreover, we found that a few of them were significantly deregulated in *Arx*-ablated cortices (Supplementary Material, Table S8 and Fig. S4A and B). Similarly, in $Arx^{(GCG)7/Y}$, we noted that genes encoding several DEPs involved in proteasome, RNA binding/splicing and translation/ribosome pathways were already expressed at the E14.5 neocortex (Supplementary Material, Table S8 and Fig. S4C and D). However, consistent with partial LoF activity of polyAla elongations, we did not observe any ARX target gene within the main pathways and cellular processes perturbed in $Arx^{(GCG)7/Y}$ brains. Based on these findings, we conclude that although most of the genes encoding the DEPs identified in our neonatal brain datasets are expressed at an early stage of corticogenesis, only a few are deregulated in the *Arx*-KO neocortex. These data might mirror distinct selective activity times of ARX in the developing brain.

Altered tubulin isotypes levels in *Arx*- mice and *C. elegans alr-1(KO)* animals

Having established by proteomic investigation a marked decrease of several tubulin isotypes in both neonatal brains, we performed western blotting to assess the total amount of α-tubulin in the $Arx^{KO/Y}$ brains with microcephaly and the $Arx^{(GCG)7/Y}$ brain with apparently normal size. In line with the proteomic datasets, a robust decrease of α-tubulin was observed in $Arx^{KO/Y}$ and $Arx^{(GCG)7/Y}$ compared to WT animals (Fig. 4B). In addition, by testing the level of the acetyl α-tubulin fraction, a severe decrease was observed in whole neonatal brains and cerebral cortices in both types of *Arx* mutant mice (Fig. 4C and D). In further work, we took advantage of the conservation of the ARX pathway between mammals and nematodes (4), and we extended our analysis to the *C. elegans alr-1(KO)* mutant. Ablated for the orthologue of *Arx*, *alr-1(KO)* animals show abnormal dendritic structures, axon guidance defects, touch insensitivity and faulty GABAergic maturation (4,24). There was a pronounced decrease in the total content of α-tubulin in *alr-1(KO)* compared to WT animals (Supplementary Material, Fig. S5A) suggesting a conserved role in the evolution of ARX/ALR-1 in regulating tubulin expression. Notably, *C. elegans* expresses nine α-tubulin isotypes (MEC-12, TBA-1, TBA-2, TBA-4 through TBA-9) involved in neurite growth, mechano- and chemo-sensation (46). In the modENCODE database, we found that two of them, *mec-12* and *tba-9*, are annotated as validated ALR-1-binding genes (Supplementary Material, Fig. S5B) (47). Very suggestively, *mec-12*, an essential gene for the generation and maintenance of the synaptic branch, is the orthologue of ARX-target gene *Tuba1a* (46,48); while *tba-9*, a gene involved in sensory cilia, is the orthologue of *Tuba4a* (49). Collectively, these findings strongly support the inference that microtubule cytoskeleton is a conserved structural network deeply damaged in *Arx* mutants. This could—at least partially—explain the neuronal abnormalities detected in $Arx^{KO/Y}$ and $Arx^{(GCG)7/Y}$, as well as those observed in *C. elegans alr-1(KO)* mutants.

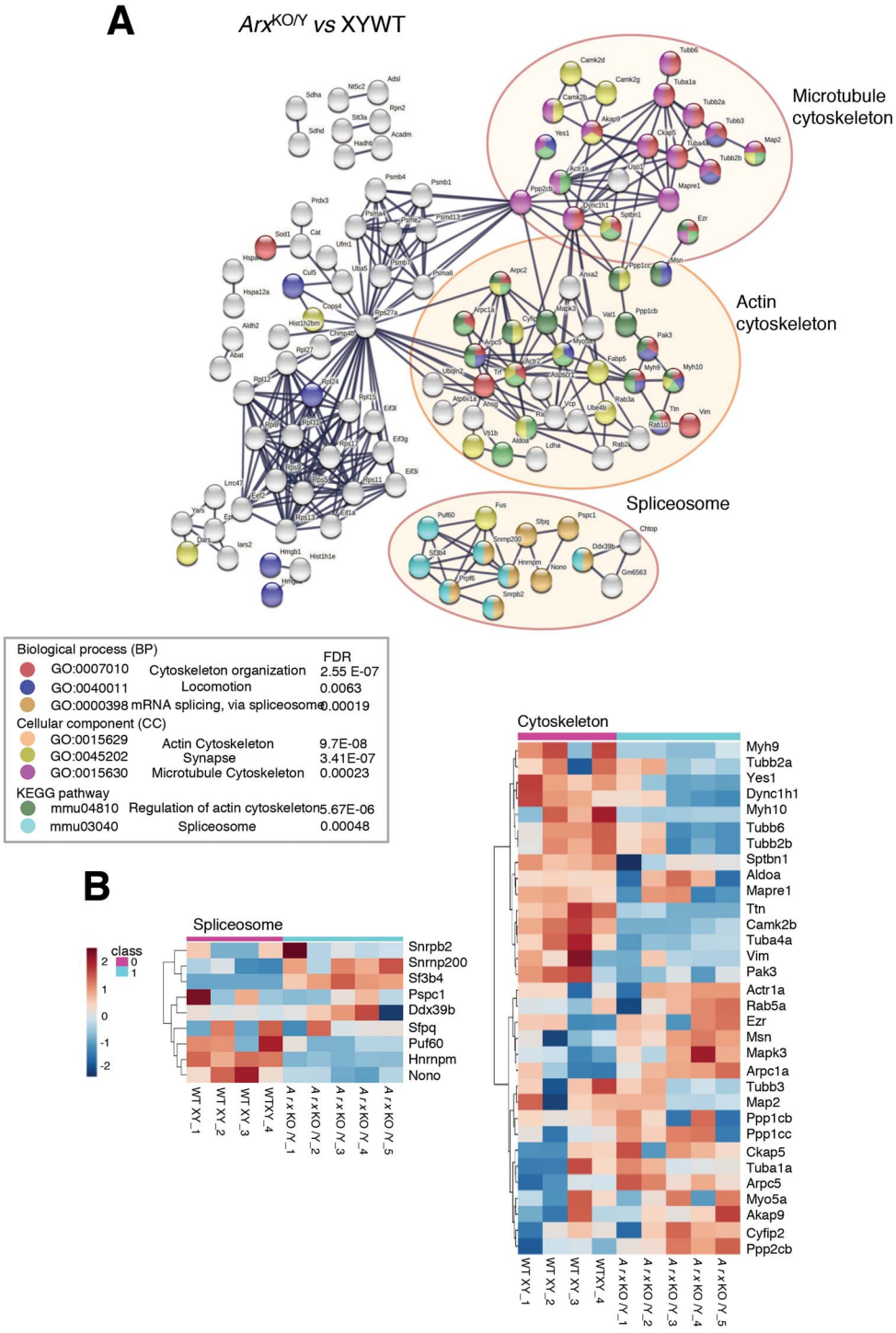

Figure 2. Functional enrichment analysis in *Arx*$^{KO/Y}$ brain proteome. **(A)** 176 deregulated proteins in *Arx*$^{KO/Y}$ were enriched for molecular processes in STRING (Search Tool for the Retrieval of Interacting Genes software) using 0.9 as the interaction score setting. Significantly enriched GO:BP, GO:CC and KEGG pathways related to cytoskeleton, locomotion, synapse structure and spliceosomes are highlighted. Each node represents a deregulated protein. **(B)** Relative abundance of splicing related proteins (left panel) and cytoskeleton proteins (right panel) in *Arx*$^{KO/Y}$ and WT XY proteomes is depicted in the heatmap where red and blue colours mean higher and lower protein abundance, respectively.

Disorganization of neurite network in Arx$^{KO/Y}$ and Arx$^{(GCG)7/Y}$ cortical neurons

As α-tubulin is central to microtubule structure and functions, we investigated the physiological consequence of the defective α-tubulin content. One of the conditions in which microtubule dynamics is functionally deregulated due to α-tubulin loss is the disorganization of the neurite network. To test this, we plated 1000 cells/mm^2 of primary cortical cells for WT, *Arx*$^{KO/Y}$ and *Arx*$^{(GCG)7/Y}$ genotypes. Confocal microscopy on *Arx*$^{(GCG)7/Y}$ and *Arx*$^{KO/Y}$ cortical neurons (DIV10) labelled with β3-tubulin revealed a drastic

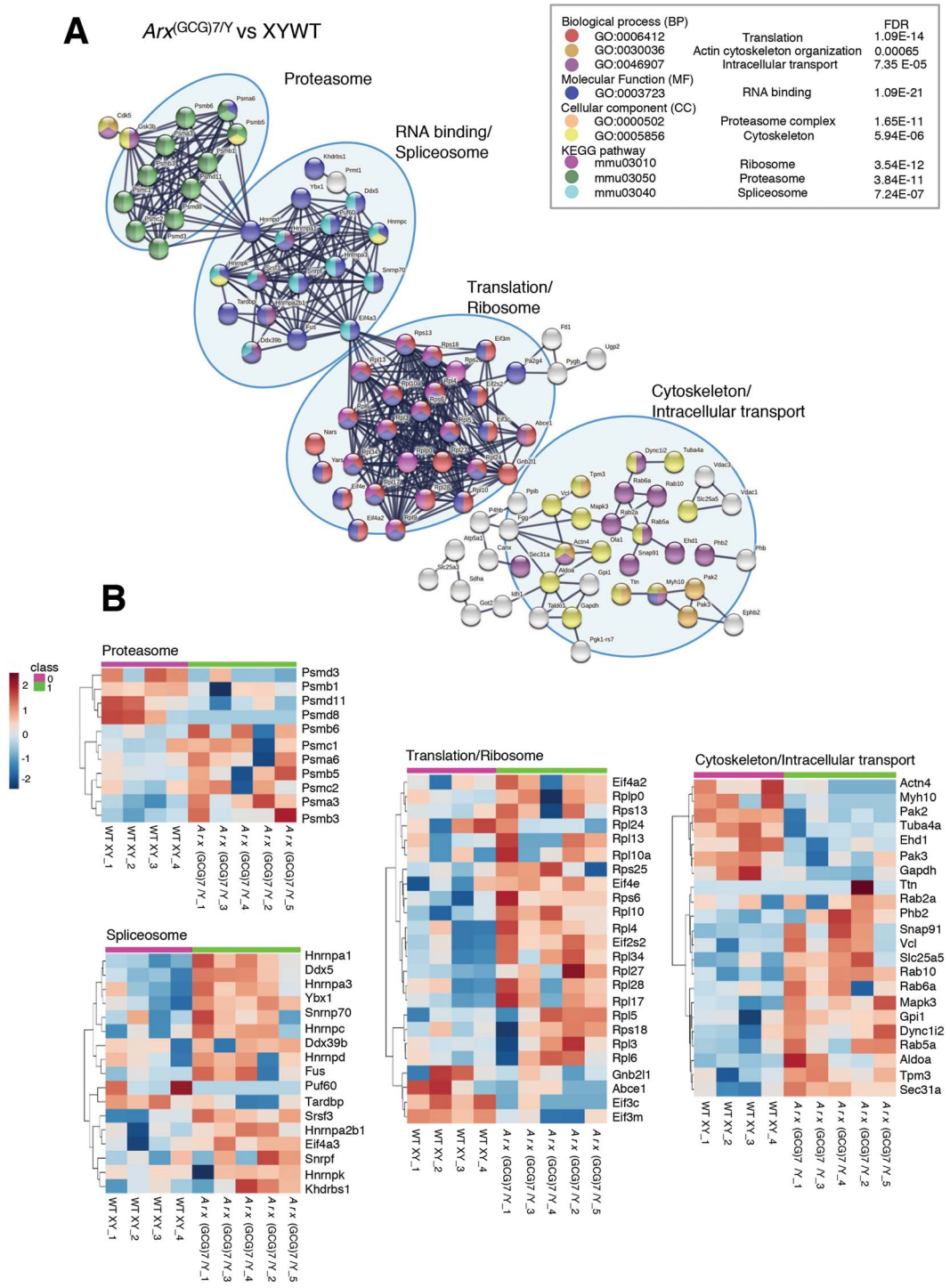

Figure 3. Functional enrichment analysis in *Arx*$^{(GCG)7/Y}$ brain proteome. **(A)** 169 deregulated proteins in *Arx*$^{(GCG)7/Y}$ were enriched for molecular processes in STRING (Search Tool for the Retrieval of Interacting Genes software) using 0.9 as the interaction score setting. Significantly enriched GO:BP, GO:CC and KEGG pathways related to proteasome, spliceosomes, ribosomes and cytoskeleton are highlighted. Each node represents a protein. **(B)** Relative abundance of DEPs belonging to proteasomes, RNA binding/spliceosomes, ribosome/translation and cytoskeleton/intracellular transport in *Arx*$^{(GCG)7/Y}$ and WT XY proteomes is depicted in heatmaps where red and blue colours mean higher and lower protein abundance, respectively.

alteration of the neurite network in both groups of mice although less severe in *Arx*$^{(GCG)7/Y}$ animals (Fig. 5A; Supplementary Material, Fig. S5C). Global disorganization of the network is obvious, with neurites entangled and randomly orientated in different directions (Fig. 5A; Supplementary Material, Fig. S5C) suggesting potential defects in axon guidance. Moreover, neurites are shorter and show aberrant variable thickness (some much thinner and others thicker in the region of cone growth) compared to the XY WT counterpart (Fig. 5A; Supplementary Material, Fig. S5C). All these findings indicate that neurite growth and arborization

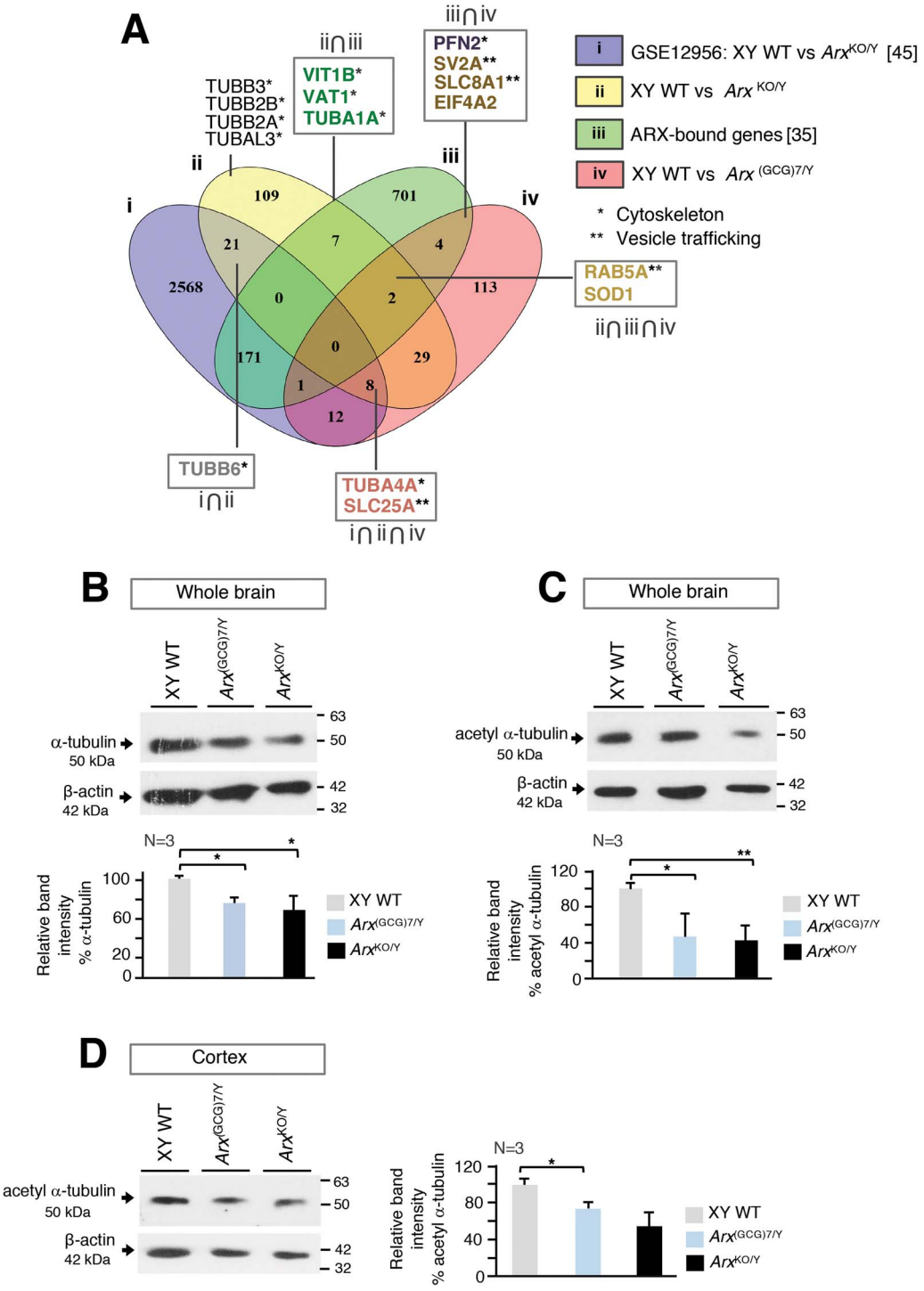

Figure 4. Defective levels of tubulin isoforms in *Arx*-disease models. **(A)** Venn diagram showing intersections of our proteome datasets with ChIP-on-chip ARX-bound genes and transcriptome data of E14.5 *Arx*-ablated cortices. Common and distinct DEPs are highlighted including those involved in cytoskeleton and vesicle trafficking (35,45). ∩ represents the intersection of gene sets. **(B)** Detection of α-tubulin levels in $Arx^{(GCG)7/Y}$ and $Arx^{KO/Y}$ whole brains. Western blot (upper panel) and band quantification (bottom panel) analysis. **(C-D)** Detection of acetyl α-tubulin expression levels in $Arx^{(GCG)7/Y}$ and $Arx^{KO/Y}$ whole brains and cortex**.** Western blot (upper panel) and band quantification (bottom panel) analysis. The western blotting experiments were repeated with five WT XY and four $Arx^{(GCG)7/Y}$ and four $Arx^{KO/Y}$ brain samples. As a loading control, β-actin was used. The band quantification of α-tubulin and acetyl α-tubulin was performed with the ImageJ 1.50i software. Columns represent mean ± standard deviation of three independent experiments per genotypes. Student's *t*-test was applied with $^{*}P < 0.05$ $^{**}P < 0.01$.

are damaged in both mice and, again, in a more severe form in $Arx^{KO/Y}$ mice. Consistent alteration of tubulin distribution/levels is clearly evident in $Arx^{(GCG)7/Y}$ and $Arx^{KO/Y}$ cortical neurons compared to XY WT in the intensity map (Fig. 5A; *lower panels*). Comparable results were obtained in immunofluorescence experiments carried out for the microtubule-associated protein 2 (MAP2): $Arx^{KO/Y}$ neurons have fewer neurites per

nucleus and some are longer than the control XY cells (Fig. 5B and C; Supplementary Material, Fig. S6). Conversely, a less severe decrease in the number of neurites per nucleus is seen for *Arx*$^{(GCG)7/Y}$ neurons (Fig. 5B and C, Supplementary Material, Fig. S6). Collectively, these data indicate that MT dynamics and neurite network are affected in both *Arx* allelic disorders, with an effect that is more pronounced in *Arx*-XLAG mice that present microcephaly than in *Arx*-DEE1 mice with apparently normal brain size.

Arx$^{(GCG)7/Y}$ mice show overexpression of eIF4A2 and evidence of impaired translation capacity

Translation is a specific cellular function that is predicted by IPA and GO analysis to be disrupted in *Arx*$^{(GCG)7/Y}$ mice brains (Figs 1 and 3). This association, reminiscent of the deficit of translation in other nucleotide repeat expansion diseases (34,50), suggests a convergent feature among them. Noteworthily, eIF4A2, which is a critical component of the CAP-dependent translation machinery particularly important in neurons (Fig. 6A) (42) was found upregulated in the *Arx*$^{(GCG)7/Y}$ proteome dataset (+ 0.4 fold; *P*-value 1.17E-02; Supplementary Material, Table S2). Thus, by western blotting we assayed the relative protein content of eIF4A2 in the whole brain and in three neonatal regions of the brain—cortex (CX), hippocampus (HP) and striatum (STR) reported as epileptogenic areas in *Arx*$^{(GCG)7/Y}$ (19). We also analysed the eIF4A2 content in the cerebellum (CB), which is a region that does not express *Arx* at any developmental stage and here used as a negative control of ARX activity (51). We found a marked eIF4a2 increase in whole brain and cortex whereas no apparent changes were observed in other brain areas analysed (Fig. 6B and C). We then asked whether the eIF4a2 increase was associated with an effect on protein translation. The surface sensing of translation (SUnSET) assay of global protein synthesis revealed a clear decrease in the total level of *de novo* proteins in *Arx*$^{(GCG)7/Y}$ primary cortical neurons compared to XY WT control neurons (Fig. 6D). Consistent with previous findings on expanded GC repeats in *C9orf72* and *FMR1* genes (50), expanded GC repeats in the *Arx* gene could induce translational suppression although further studies are needed to deeply define the molecular basis of these phenomena.

Alterations of splicing switches in *Arx*- mice and *C. elegans alr-1*(*KO*) animals

Going into the details of IPA analysis, with reference to RNA splicing in *Arx*$^{KO/Y}$ and *Arx*$^{(GCG)7/Y}$ datasets, 8 and 15 DEPs were identified respectively (Fig. 7A). Very interestingly, previous studies carried out in *C. elegans alr-1*(*KO*) mutants revealed a role of ARX/ALR-1 in single-neuron gene splicing (52). Based on this evidence, we asked whether alternative splicing (AS) regulation might be a conserved ARX function. Initially, by quantitative western blotting analysis, we validated the decrease of PUF60, a common downregulated transactivating splicing factor in *Arx*$^{(GCG)7/Y}$ (– 4.4 fold; *P*-value 1.61E-02; Supplementary Material, Table S1) and *Arx*$^{KO/Y}$ (–2.2 fold; *P*-value 5.53E-02; Supplementary Material, Table S2) neonatal whole brain (Supplementary Material, Fig. S7A). Next, to investigate the influence of PUF60 decrease on AS, we assayed the abundance of PUF60-activated AS for three genes—*hnRNPD, hnRNPC* and *hnRNPK*—which in turn control alternative and constitutive pre-mRNA splicing (53). By semiquantitative PCR, we tested the two AS isoforms e6(+) and e6(–) of *hnRNPD*, generated by the skipping or inclusion of exon 6 respectively; the two AS isoforms e14b(+) and e14b(–) of *hnRNPK*, generated by the skipping or inclusion of exon 14b respectively; and the two AS isoforms e4(+) and e4(–) of *hnRNPC*, generated by the skipping or inclusion of exon 4 respectively (Fig. 7B). There were no differences in the AS ratio in the whole brain of DEE1 mice compared to the XY mice (Supplementary Material, Fig. S7B), but we detected an increase of *hnRNPD* e6(+)/e6(–) and of *hnRNPC* e4b(+)/e4b(–) AS ratio in HP whereas no apparent changes in the *hnRNPK* e14b(+)/e14b(–) AS ratio were observed (Fig. 7C and D). In addition, no changes were observed in CB samples used as negative controls of ARX activity.

As alternative splicing governs mammalian brain development, we further corroborated experimentally our proteomic data analysis by verifying the impact of the increase of SAM68 found upregulated in the *Arx*$^{(GCG)7/Y}$ dataset. For this purpose, we took advantage of the fact that SAM68 directly binds RNA recognition motifs in the introns flanking the highly conserved alternative exon at splice site 4 (AS4) of pre-mRNAs for *Neurexin-1* (*Nrxn1*) (54). Remarkably, *Nrxn1*—together with *Nrxn2* and *Nrxn3* genes—belongs to the *Neurexin* gene family involved in epilepsy, autism and schizophrenia (54). A genetic feature of the *Neurexin* family of genes is the extensive alternative splicing they undergo generating distinct transcription isoforms encoding a wide range of presynaptic receptors involved in synapse remodelling. In particular, incorporation or skipping of exon 22 at AS4 generates multiple NRXN AS4(+) and NRXN AS4(–) variant proteins (55,56). These isoforms exhibit differential interactions with several ligands mediating synaptogenesis including neuroligins (NLGS) and leucine-rich repeat proteins (Fig. 8A) (55,56). Although SAM68 specifically regulates AS4 of *Nrxn1*, we also analysed AS4 of *Nrxn2* and 3 to obtain more information about the splicing control of this family given its involvement in neurological disorders. By semiquantitative PCR assay, we tested the abundance of AS4(+) and AS4(–) of *Nrxn1, 2* and 3 in whole brain and dissected areas of *Arx*$^{(GCG)7/Y}$ mice. We detected a significant increase in the *Nrxn2* AS4(+)/*Nrxn2* AS4(–) ratio but no differences in the *Nrxn1* AS4(+)/*Nrxn1* AS4(–) and *Nrxn3* AS4(+)/*Nrxn3* AS4(–) ratio were found in the whole brain of DEE1 mice compared to the XY mice (Supplementary Material, Fig. S7C). More importantly, in the dissected *Arx*$^{(GCG)7/Y}$ areas there was a significant

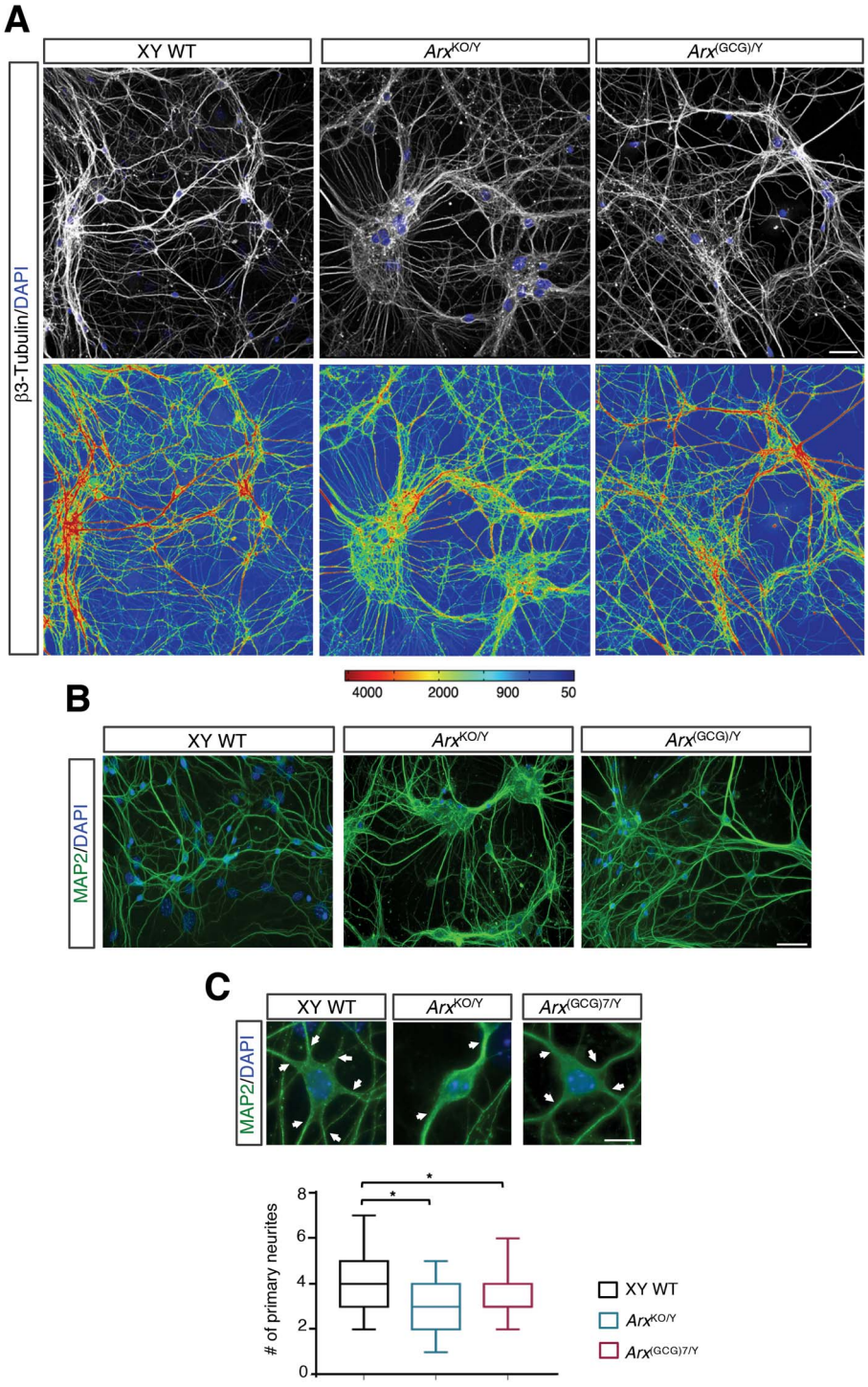

Figure 5. Neurite network in $Arx^{(GCG)7/Y}$ and $Arx^{KO/Y}$ primary cortical neurons. **(A, B)** Representative immunofluorescence of $Arx^{(GCG)7/Y}$ and $Arx^{KO/Y}$ primary cortical neurons cultured in NB. DIV 10 cells were fixed and stained with β-III tubulin (red) and DAPI (blue) (**A**) and with MAP2 (green) and DAPI (blue) (**B**). **(C)** Quantification of the number of primary neurites in XY WT ($N = 57$ cells), $Arx^{KO/Y}$ ($N = 53$ cells) and $Arx^{(GCG)7/Y}$ ($N = 62$ cells) primary cortical neurons from two independent experiments. Whisker plots represent median with min to max values. One-way ANOVA with Dunn's multiple comparisons was applied with $^*P < 0.05$. In (A), images were acquired with a confocal microscope taking Z-slices from the top to the bottom of cells; the 3D reconstruction and the corresponding intensity maps are shown. Scale bars represent 5 μm in (A) (original magnification ×20); 50 μm in (B) (original magnification ×40); and 10 μm in (C) (original magnification ×100). Arrows indicate primary neurites.

higher level of *Nrxn1* AS4(+)/*Nrxn1* AS4(−) ratio in CX and HP but decreased in STR (Fig. 8B and C). In line with the whole brain data, a significant higher level of *Nrxn2* AS4(+)/AS4(−) ratio was found in HP; and finally, *Nrxn3* AS4(+)/AS4(−) ratio was significantly higher in CX (Fig. 8B and C).

Given the crucial role of Neurexins in synaptogenesis and that several DEPs of $Arx^{KO/Y}$ dataset are involved

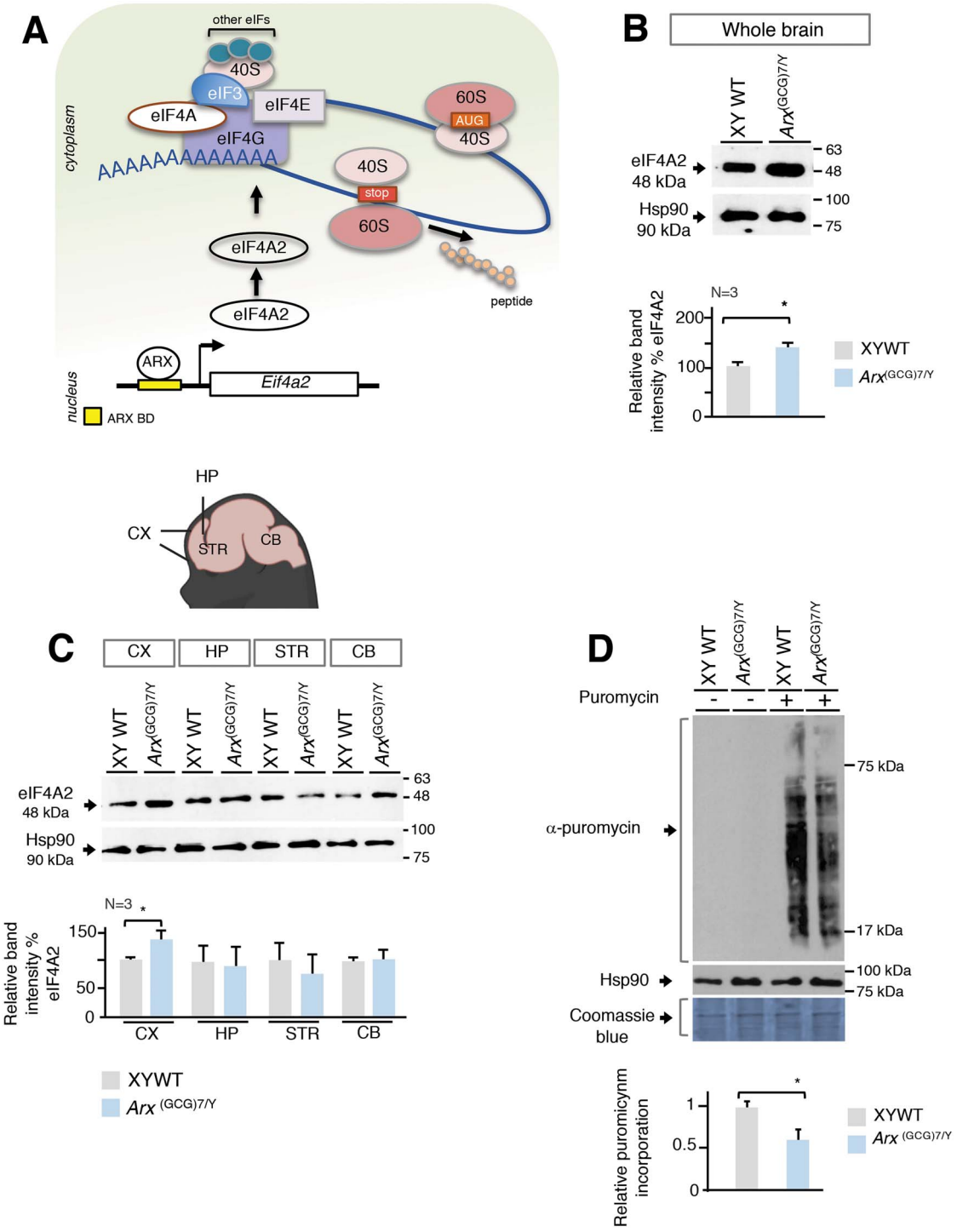

Figure 6. Analysis of eIF4A2 levels in *Arx*$^{(GCG)7/Y}$ brain and of global protein synthesis in *Arx*$^{(GCG)7/Y}$ primary neurons. (**A**) Schematic representation of translation initiation. eIF4A2 is an RNA helicase ATP-dependent protein encoded by the *Arx* target gene *Eif4a2* involved in the first step of translation. (**B**, **C**) Detection of eIF4A2 expression levels in whole brain and dissected areas of *Arx*$^{(GCG)7/Y}$. Western blot (*upper panel*) and band quantification (*bottom panel*) analysis. As loading control, Hsp90 antibody was used. Student's *t*-test was applied with $^{*}P < 0.05$. Schematic depiction of mouse brain regions used for eIF4A2 expression analysis is shown. CX, cortex; HP, hippocampus; STR, stratum; CB, cerebellum. (**D**) Western blotting-SUnSET analysis of primary cortical neuron lysates from XY WT and *Arx*$^{(GCG)7/Y}$ untreated and puromicyn treated cells. Equal loading was confirmed with coomassie blue staining**.** Quantitative representation of puromycin incorporation is expressed as the fold change relative to XY WT cells. $n = 3$ neuronal cell cultures per genotype. Data are presented as mean ± SD and Student's *t*-test was applied with $^{*}P < 0.05$.

in RNA splicing control, we asked whether CX, HP and STR of XLAG mice might present an altered AS profile of *Neurexins*. Surprisingly, we noted only a significant decrease of *Nrxn3* AS4(+)/AS4(−) ratio in the control brain area of CB (Supplementary Material, Fig. S7D). Altogether, these findings suggest that changes of *Neurexins* repertoire in the epileptogenic areas of *Arx* polyalanine mice are strictly genotype dependent and can be

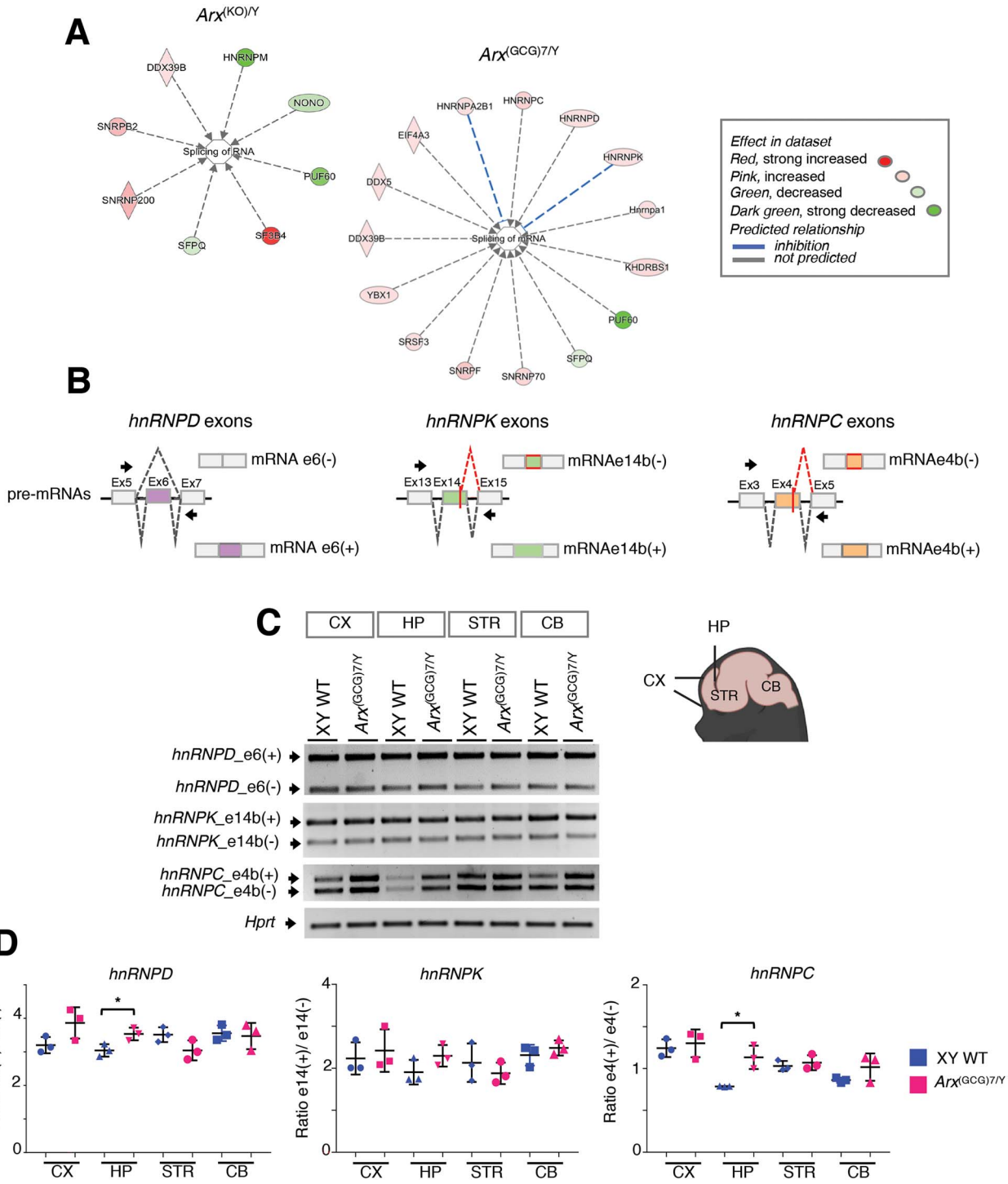

Figure 7. Network of mRNA splicing in *Arx* mutant mice and analysis of splicing events in *hnRNP* genes. (**A**) Network of mRNA splicing in $Arx^{KO/Y}$ and $Arx^{(GCG)7/Y}$ datasets were generated through IPA (QIAGEN Inc., https://www.qiagenbioinformatics.com/products/ingenuity-pathway-analysis/). (**B**) Schematic diagrams outlining organization of splicing variants of *hnRNPD* (exon 6), *hnRNPK* (exon 14b) and *hnRNPC* (exon 4b) are shown. Arrows indicate the positions of oligonucleotides used in transcript analysis. (**C**) Semiquantitative PCR analysis with primers for *hnRNPD* AS exon 6 (e6+), *hnRNPK* AS exon 14b (e14b+) and *hnRNPC* AS exon 4b (e4b+) in dissected brain areas of $Arx^{(GCG)7/Y}$. (**D**) Ratio of band quantification of AS e(+)/AS e(−) is plotted. Columns represent mean ± SD of three independent tissues samples *per* genotype. Student's *t*-test was applied with $^*P < 0.05$. CX, cortex; HP, hippocampus; STR, stratum; CB, cerebellum.

considered a secondary effect of the polyalanine-elongated variant. Nevertheless, why we detected the aberrant ratio of *Nrxn3* isoforms only in CB of $Arx^{KO/Y}$ remains to be explored. One possible explanation is that the null allele of *Arx* could have a direct or indirect impact on downstream diffusible long-range effectors—secreted outside the ARX-expressed areas—with a key role in CB plasticity. However, a proper dynamic splicing program of Neurexins is required to control synaptogenesis in cerebellar neurons (57).

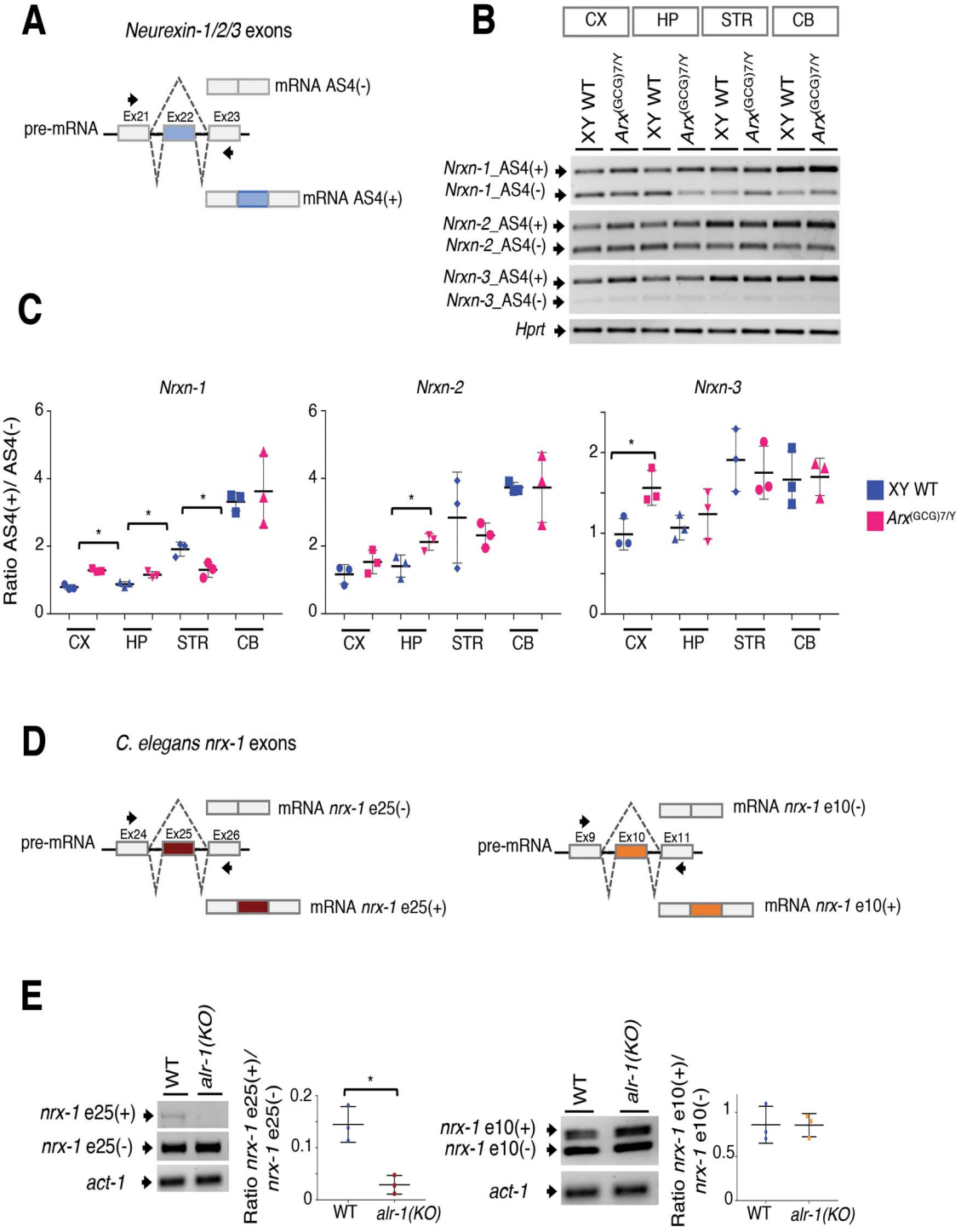

Figure 8. Analysis of *Neurexins* alternative splicing in $Arx^{(GCG)7/Y}$ and $Arx^{KO/Y}$ mice and in *C. elegans alr-1*(*KO*). (**A**) Schematic representation of exon 22 splicing in murine *Nrxn1/2/3* genes. Arrows indicate the positions of oligonucleotides used in transcript analysis. **(B)** Semiquantitative PCR analysis with primers to detect *neurexin1/2/3* AS4 in $Arx^{(GCG)7/Y}$ dissected areas. (**C**) Ratio of band quantification of AS 4(+)/AS 4(−) is plotted. Columns represent mean ± SD of three independent tissues samples *per* genotype. CX, cortex; HP, hippocampus; STR, stratum; CB, cerebellum. Student's *t*-test was applied with $^*P < 0.05$. (**D**) Schematic representations of exons 25 and 10 splicing in the *C. elegans nrx-1* gene. Arrows are primers used for semiquantitative PCR analysis. (**E**) Semiquantitative PCR analysis with ratio of bands to quantify the alternative isoforms of *nrx-1* e25(+), e25(−) (left panel), e10(+) and e10(−) (right panel) in *alr-1*(*KO*) L4 larvae mutants. PCR amplicons were run on 2.5% agarose gel, densitometric analysis was performed with the ImageJ software and quantification of the ratio of *nrx-1* e(+)/(−) abundance was plotted. Student's *t*-test was applied with $^*P < 0.05$.

Likewise in mammals, the single *C. elegans* orthologue of mammalian *Neurexins*, *nrx-1*, controls synaptic remodelling (58) and encodes several isoforms that are temporally controlled (54,59). Although *C. elegans* lacks a SAM68 orthologue, a sequence homologous to *Nrxn1* splice acceptor sequence AS4, which is recognized by SAM68, has been identified in *nrx-1* intron 24 (Supplementary Material, Fig. S8) (60). We assayed the

two *nrx-1* transcript isoforms *nrx*-1 e25(−) and *nrx*-1 e25(+) generated by the skipping or inclusion of exon 25 of *nrx-1*, respectively (Fig. 8D). There was a high level of *nrx*-1 e25(−) coupled with a drastic decrease of *nrx-1* e25(+) in *alr-1*(*KO*) mutants and a significantly decreased ratio of the band quantification of *nrx-1* e25(+)/*nrx-1* e25(−) (Fig. 8E left panel). We furthered the analysis by testing two *nrx-1* transcript isoforms *nrx-1* e10(−) and *nrx*-1 e10(+), generated by the skipping or inclusion of exon 10 that is not surrounded by splicing sequences homologous to the SAM68 binding site (Fig. 8D). We observed no change in the *nrx-1* e10(+)/*nrx*-1 e10(−) ratio in the *alr-1*(*KO*) animals compared to WT (Fig. 8E; right panel). We therefore suggest that *alr-1* has an exon-specific role in regulating *nrx-1* e25 isoforms. In contrast, a different molecule or mechanism is the basis of generation of the *nrx-1* e10 isoforms. Collectively, our findings point to a new and unanticipated evolutionary conserved *Arx*-dependent mechanism accounting for alternative splice regulation choice of the *Nrxn* gene. As NRXN1 AS4(+) and AS4(−) isoforms exhibit differential adhesion/binding with NLGs (e.g. neuroligin 1B postsynaptic receptor weakly binds AS4(−) but AS4(+) strongly) (59), we infer that the expression of an altered Neurexin-1 repertoire might lead to a synaptopathy due to improper axo-dendritic interactions.

Neurexin AS4 splicing in *Arx*$^{(GCG)7/Y}$ depolarizing cortical neurons

Next, we asked whether an altered Neurexin repertoire might impair the neuronal activity in *Arx*$^{(GCG)7/Y}$, the transgenic mouse with spontaneous recurrent seizures. As a high K^+-induced depolarization of the neuronal membrane induces a change of synaptic plasticity through an increase of *Nrxn1* AS4(+)/AS4(−) ratio (Fig. 9A) (54), we analysed the physiological consequences of this phenomenon in the *Arx*$^{(GCG)7/Y}$ primary cortical neurons (Fig. 9B). First, primary neuron cultures from *Arx*$^{(GCG)7/Y}$ and XY WT pups were depolarized with elevated KCl. Successively, we carried out transcript analysis of *Nrxn-1* AS4 isoforms and of *c-fos* whose increase is generally used to validate induction of synaptic plasticity in response to a stimulus (Fig. 9C) (54). As expected, KCl-treated XY WT neurons exhibited a significant upregulation of *c-fos* and of *Nrxn1* AS4(+)/AS4(−) ratio compared to resting (not-treated) XY WT cells (Fig. 9C–E). Conversely, there were reduced levels of *c-fos* and of *Nrxn1* AS4(+)/AS4(−) ratio both in resting and KCl-treated *Arx*$^{(GCG)7/Y}$ cortical neurons compared to the control cells (Fig. 9C–E). Expanding our analysis to AS4 of *Nrxn* 2 and 3, there was only a modest increase of *Nrxn2* in *Arx*$^{(GCG)7/Y}$ KCl-treated cortical neurons compared to the resting cells (Fig. 9D and E). In sum, these findings depict a pathogenetic feature that might affect the electrical activity of *Arx*$^{(GCG)7/Y}$ neurons and thus contribute to the DEE1 phenotype.

Discussion

We report an extensive proteomics analysis to reach a consensus view of changes in brains of XLAG and DEE1 mouse models compared to wild-type. We find that most of DEPs and enriched pathways are consistent with pleiotropic defects reflecting overlaps between the two ARX-endophenotypes as well as genotype-dependent differences (Fig. 10). This permitted us to identify functional alterations affecting microtubule network and RNA metabolism, some of them related to defects previously described in *ARX* patients and mouse models and also involved in other neurological disorders (29,30,33,54).

Microtubule network deregulation. One of the most interesting observations of our study concerns several DEPs related to microtubule (MT) structure and functioning found in *Arx*-XLAG and DEE1 pup brains. MTs are built of α and β-tubulin heterodimers that self-assemble head-to-tail into protofilaments and are required to establish correct brain development and network connectivity (30,33,61–63). In both *Arx*- mice models we detected a robust decrease of α-tubulin global content and α-tubulin acetylation associated with defective neurite growth and arborisation (37,64–66). Furthermore, the clear reduction of α-tubulin in the *C. elegans Arx/alr*-KO mutant model and the evidence that two α-tubulin isotype genes, *mec-12* and *tba-9*, are ALR-1 targets suggest a conserved role of ARX/ALR-1 in regulating tubulin expression. These data allow us to discover a new disease phenologue pathway in addition to the one we identified earlier (4). Notably, MTs provide a mechanical force for the remodelling of adherens junctions (AJs) and cell–cell adhesions: the former is the most perturbed pathway in *Arx*$^{KO/Y}$ and the latter is one of main biological process damaged in *Arx*$^{(GCG)7/Y}$ neonatal brain. As AJs and cell–cell adhesions ensure the fidelity of neural network development, failures in their assembly and disassembly could underlie the defective neurogenesis and synaptogenesis detected in *Arx* disease mice (25). Moreover, cytoskeleton, migration and neuronal plasticity—which are among the top-ranked terms identified in our proteomic datasets—have been functionally linked to the anatomic defects and neuronal migration alterations previously described in *ARX* patients (29,67–71).

Nevertheless, these functions were also linked to the aberrant corticogenesis and defective neuronal maturation detected in *Arx* mutant brains (17,69,72,73). Related to these evidences, the decreased amount of α-tubulin observed by us in *Arx*$^{KO/Y}$ and *Arx*$^{(GCG)7/Y}$ brain could explain the defective connectivity and axonogenesis detected—even if at different level of severity—in *Arx* mutant mice and *ARX* patients (17,69,72).

Furthermore, this hypothesis is reinforced by our findings in *C. elegans* mutants. Indeed, the abnormal dendritic structures previously observed in three different classes of *alr-1* KO neurons, which are involved

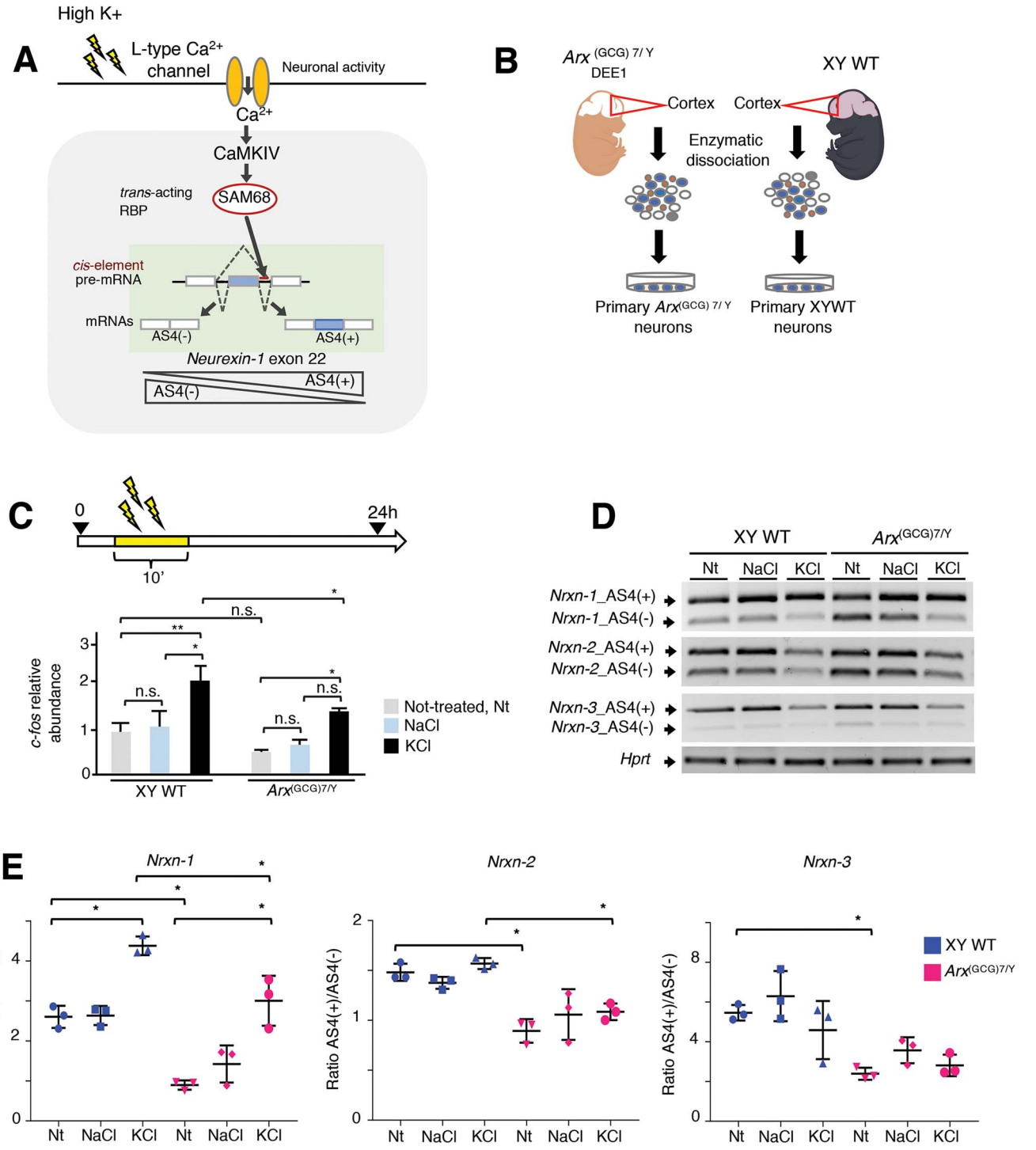

Figure 9. Changes of *neurexin* 1/2/3_AS4 splicing induced by depolarization in $Arx^{(GCG)7/Y}$ primary cortical neurons. **(A)** Model of the *neurexin* AS4(+) and AS4(−) isoform splicing stimulated by neuronal activity *via* SAM68. High K^+-induced depolarization triggers a shift in the alternative splicing within cultured neuronal cells *via* Ca^{2+}/calmodulin-dependent kinase IV (CaMKIV) (54) that is thought to activate the splicing factor SAM68. Specifically, this RBP activates a shift in the alternative splicing of *neurexin* pre-mRNA that contains the SAM68-consensus recognition motif (in red). Constitutive levels of *Nrxn* AS4(+) are low in primary cortical neurons and increase upon depolarization. **(B)** Schematic depiction of isolation of primary cortical neurons from $Arx^{(GCG)7/Y}$ and XY WT pups. **(C)** Quantitative real-time PCR of *c-fos* in resting (not-treated) and depolarized neurons treated with NaCl or KCl for 10 min. Two-way ANOVA with Tukey's multiple comparisons test was applied with $^*P < 0.05$, $^{**}P < 0.001$. **(D)** Semiquantitative RT-PCR of alternative isoforms of *Nrxn* 1/2/3_AS4 in resting and NaCl- or KCl-depolarized cortical neurons. (**E**) Ratio of band quantification of AS 4(+)/AS 4(−) is plotted. Columns represent mean ± SD of three independent tissues samples. Two-way ANOVA with Tukey's multiple comparisons test was applied with $^*P < 0.05$.

in olfaction, thermo-sensation and chemo-sensation (24), could be the consequence of an altered dendrite growth caused by an insufficient amount of α-tubulin. Remarkably, mutations in the human counterpart of several tubulin isotypes found deregulated in *Arx* mice (i.e. TUBA1A, TUBA4A, TUBB2A and TUBB2B) lead to a wide spectrum of severe brain malformations known as 'brain tubulinopathies' presenting lissencephaly and

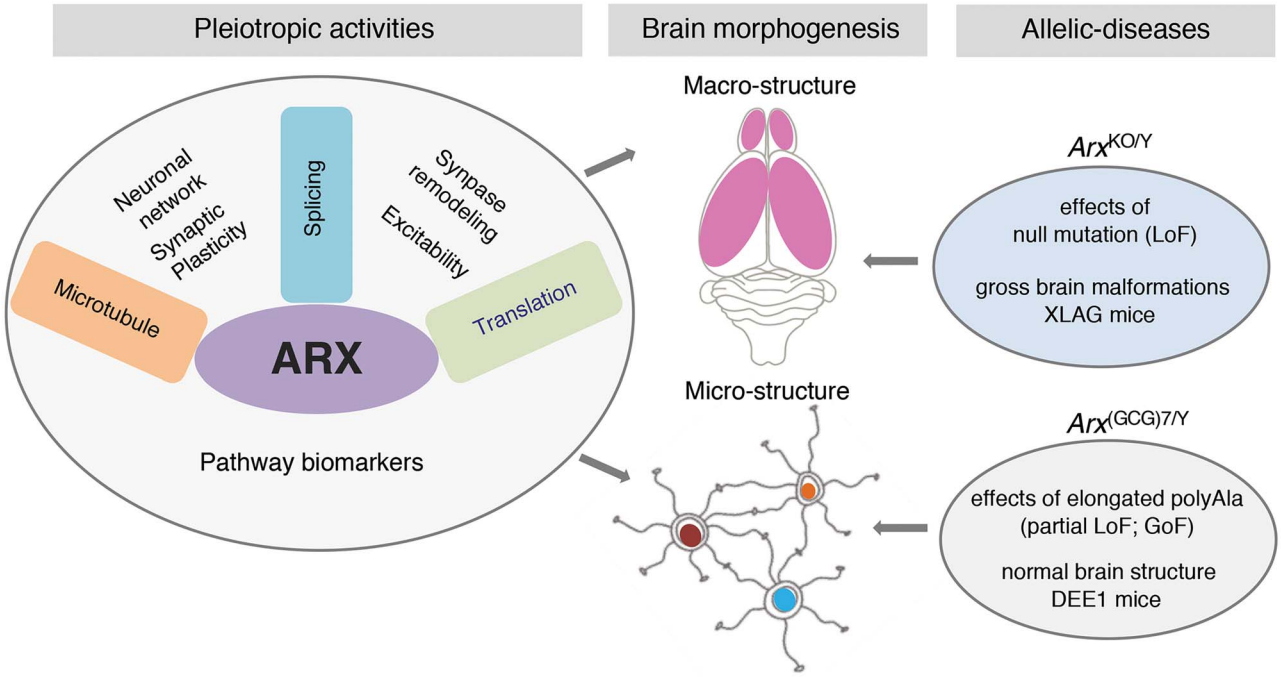

Figure 10. Secondary ARX-related alterations highlighted in *Arx*-allelic disorders and involved in macro- and microstructures of the developing brain.

basal ganglia defects (33,62,63). These clinical features overlap with similar anatomic defects described in *ARX* patients (10,29,68) suggesting that these NDDs share common comorbidities and thus disease hallmarkers.

No less important is the defective level of acetylated α-tubulin detected in both conditions that, as already proved, alter axon branching and neuronal microcircuitry (74–77). We have no evidence that a faulty process common to both mouse models directly compromised acetylation levels, but one can envisage a negative regulatory feedback loop that could control the levels of acetylated-α-tubulin. About the morphological changes of neurite network observed in the primary cortical cultures of both *Arx* mutants, we infer that they could be the resultant of multiple defects affecting microtubule assembling. These results are in line with the previous findings on the cell-autonomous activity of ARX into regulating the morphology of pyramidal cells (16) that are the main component of primary cortical cells (78). We therefore conclude that the two *Arx* endophenotypes analysed are two distinct secondary brain tubulinopathies whose pathogenicity depends on the extent of MT impairment: more extensive in $Arx^{KO/Y}$ and relatively constricted in $Arx^{(GCG)7/Y}$. This conclusion correlates with the poorly developed perinatal $Arx^{KO/Y}$ brain (17,18) and the abnormal axonal arborization and hyperexcitability of $Arx^{(GCG)7/Y}$ mice (27).

RNA metabolism deregulation. Understanding the cellular and molecular pathophysiology of *Arx* polyalanine mice remains a challenge. In particular, to establish whether protein aggregation might increase the severity of the phenotype because it adds a possible gain-of-function to a partial loss of function mechanisms could be relevant to identify appropriate therapeutics. Previous studies carried out by us and others have shown that expansions of polyAla stretches found in DEE1 patients lead to intranuclear protein inclusions consequent of protein misfolding and aggregation (2,3,15). Our brain proteome data for *Arx*-DEE1 mice provide the first evidence that pathways strongly interconnected with the integrated stress response (ISR), a cellular process that controls protein folding (79–83) and involved in trinucleotide repeat expansion disorders (84,85), are highly affected. Indeed, *eIF2* signalling is the most enriched pathway in $Arx^{(GCG)7/Y}$ neonatal brain, along with the regulation of *eIF4* and *p70S6K* and *mTOR* signalling (79–83). Suggestively, one of the DEPs involved in these processes is eIF4A2, a subunit of the eIF4F complex required for mRNA binding to ribosomes (42,82,86,87). It is encoded by an ARX target gene that is highly expressed at the early stage of embryonic brain development. In addition, the eIF4A2 overexpression coupled with the translational suppression detected in $Arx^{(GCG)7/Y}$ overlaps with similar findings reported in other neurological repeat expansion disorders (34,50). Finally, excessive levels of eIF4A2 have been reported acting as a memory repressor blocking long-lasting forms of synaptic plasticity (82,83,88), a manifestation that correlates well with the behavioural profile of $Arx^{(GCG)7/Y}$ mice (19). Moreover, translation and proteasome function as well as protein ubiquitination—which are among the top-ranked terms identified in *Arx* polyalanine brains—have been previously related to the protein aggregation caused by *ARX* polyalanine elongations (15). These

results reinforce our hypothesis on the gain-of-function effect of *Arx* (GCG)7 mutation. Although further studies focused on GCG repeats in ARX are needed, we therefore conclude that misfolded *Arx* polyalanine elongations might activate a pathogenic mechanism affecting the translation of mRNA.

Another essential mechanism of RNA metabolism affected in *Arx* polyalanine brains is the control of alternative splicing (AS), a complex phenomenon widely observed at high frequency during brain development, whose misregulation affects synapse plasticity and promotes neuronal hyperexcitability (89–92). This is a current active area of research. The enrichment of DEPs involved in AS detected in *Arx*-XLAG and *Arx*-DEE1 pup brains reveals an unexpected molecular scenario that links ARX pathology to AS mis-regulation. As proof-of-concept, we detected defective splicing patterns in a subset of pre-mRNAs that are specific targets of the two DEPs PUF60 and SAM68. Those two splicing factors are both involved in human NDDs. PUF60, a regulatory player of the 3-prime splice site recognition, is encoded by a gene found mutated in patients presenting developmental delay, microcephaly, seizure and skeletal abnormalities (Verheij syndrome, VRJS; MIM 615583) (89). SAM68 is a regulator of activity-dependent AS of *Neurexin*-1, a gene encoding multiple isoforms of the presynaptic receptor Neurexin-1 and whose mutations have been repeatedly associated with ID, epilepsy, autism and schizophrenia (44,93,94). In $Arx^{(GCG)7/Y}$ hippocampus we detected an aberrant splicing ratio of two PUF60 targets *hnRNPD* and *hnRNPC* encoding variant isoforms of these two hnRNPs with many effects on macromolecular dynamics (i.e. DNA replication, transcription and chromatin remodelling); RNA (i.e. mRNA stability and RNA splicing); and protein levels (translation and degradation) (95,96). How these AS abnormalities might impact physiologically on ARX-dependent physiology and contribute to XLAG and DEE1 disease phenotypes is not clear. Instead, even though progress has been made in the understanding of hnRNP action, its functions in brain deserve further investigation. More interestingly, aberrant *Nrxn* AS4(+)/*Nrxn* AS4(−) ratios of the SAM68 target *Nrxn1* were observed in the epileptogenic niches of $Arx^{(GCG)7/Y}$ mice (cortex, hippocampus and striatum), where seizures jointly start in young animals (19). As these brain areas differ both in ARX expression and neuronal subtype composition (51,97), further studies are required to establish whether the defective NRXN1 repertoire might alter the cell fate in the developing cerebral areas. We therefore infer that ARX is involved in the AS programs of *Nrxn1* in important brain areas of DEE1 mice.

A further confirmation of the crucial role of ARX in AS was obtained in *alr-1* (*KO*) worms, in which an altered AS ratio of the *Nrxn 1* orthologue was found at the predicted SAM68-binding site. These data, together with the recent findings on the regulatory role of ARX/ALR-1 in splicing in a single *C. elegans* neuron (52), suggest that ARX is an evolutionarily conserved regulator of AS.

Very important, in addition to participating in the specification of cellular identity, the *Nrxn* splice repertoire—through dynamic regulation—changes in response to neuron signalling (54,98). Specifically, strong pharmacological or electrical stimulation can induce shifts in the *Nrxn* AS4(+)/*Nrxn* AS4(−) ratio (54,98). In the present study, we have discovered a defective increase of AS4(+)/AS4(−) ratio of *Nrxn1* associated with a marked defective plasticity of $Arx^{(GCG)7/Y}$ cortical neurons, as evidenced by faulty expression of the firing activity marker *c-fos*. Considering that neurexins are central regulators of synapse properties, it is reasonable to link the faulty neuronal response and defective splicing. This adds to a substantial body of literature findings that deficiency in the neurexin repertoires can induce behavioural alterations and hyperactivity in rodents (55). Overall, our data explain much of the catastrophic effect of faulty ARX action and shed light on a new function of ARX in controlling AS. This interesting finding opens up further studies aimed at defining the temporal regulation of AS in brain areas of *Arx* mutant mice. To this end, single-cell RNA sequencing analysis could provide new insights into the global spliceosome activity of ARX, for example, whether ARX controls splice isoform switching during neural development and how it contributes to defining neuronal maturation stages and cellular heterogeneity (92). Remarkably, we discovered a new aspect of ARX pathophysiology involving defects in the combinatorial codes of cell adhesion molecules Neurexin 1 and 2 (55–57), a class of presynaptic proteins that are required for efficient neurotransmission and formation of synaptic contacts (98). As their corresponding human genes were found involved in neurodevelopmental disorders (54,93), it will be interesting to establish how, when and where these processes contribute to the triggering and evolution of epileptogenesis.

In conclusion, we infer that depending on the pleiotropic impact of the null or the polyalanine expansion mutations on the genetic program controlled by ARX, defects in microtubule organization, translation efficiency and splicing patterns converge to generate macro or micro defects in *Arx*-XLAG and *Arx*-DEE1 pup brains. Of significance, in this study we highlight the GoF activity of the expanded repeat mutation *Arx* (GCG)7 by shedding light on an unclear aspect of the pathophysiological consequences of this polyalanine expansion. However, it remains to be determined whether all the expansion mutations found in *ARX* patients (2,8,10) and modelled in mice (7,13,15,21,27) have a GoF effect or whether there is a relationship dependent on the affected polyAla tract (first or second) or on the number of added alanine codons.

Taken together, these findings led to the identification of novel ARX-related pathway biomarkers opening up to new studies in attempts to find

molecular-guided therapy. This could have important applications for both ARX-endophenotypes and NDD with overlapping comorbidities such as lissencephaly and epilepsy caused by mutations in tubulin isoform genes (brain tubulinopathies) (63), basal ganglia disorders (29) and autism spectrum disorders associated with *NRXN1* variants (93).

Materials and Methods

Mouse welfare and ethical statements

All experiments in mice were conducted in conformity with the European Community Directive 2010/63/EU and were approved by the Italian Ministry of Health (D.L.gs n. 26/2014) in accordance with the institutional animal care guidelines of the Institute of Genetics and Biophysics 'Adriano Buzzati-Traverso', under the accreditation n°307/2018-PR and n° 0009895-P.

Animal models

$Arx^{KO/Y}$ knockout colony was kindly provided by Dr Collombat (99). $Arx^{(GCG)7/Y}$ knock-in colony was purchased from the RIKEN BioResource Center in Japan (strain name: *Arx*(GCG)7–1 KI (B6), RBRC03654). Mice were maintained by crossing heterozygous females $Arx^{(GCG)7/X}$ with WT males C57BL/6 J and $Arx^{KO/X}$ with WT males C57BL/6 J (*Arx* is on the X-chromosome). $Arx^{(GCG)7/Y}$ genotyping was performed according to the protocol of the RIKEN BioResource Center (19) and $Arx^{KO/Y}$ genotyping was made according to the protocol described in Collombat et al. (99) using oligonucleotide primer pairs listed in Supplementary Material, Table S9. Sex assessment of male pups was performed by PCR amplification of the *Sry* gene using the pair of oligos reported in Supplementary Material, Table S9. $Arx^{KO/X}$ and $Arx^{(GCG)7/X}$ heterozygous female pregnancy was assessed after overnight mating and embryonic age was calculated as E0.5 when the vaginal plug was detected. Mice were sacrificed at birth upon deep anaesthesia with isoflurane. Whole brain and brain sections were dissected from XY WT, $Arx^{KO/Y}$ and $Arx^{(GCG)7/Y}$ animals under a stereomicroscope and then snap-frozen in liquid nitrogen (100). *C. elegans* animals were grown and handled following standard procedures at 20°C, on nematode growth medium (NGM) agar plates seeded with *Escherichia coli* strain OP50 (101). For *alr-1*(*oy42*), a null mutant hence referred as *alr-1*(*KO*), the genotype was determined by PCR as described in Poeta *et al.* (4).

Proteome extraction and sample preparation

Whole frozen brain tissues were mechanically disrupted following the procedure elsewhere described (64,102). Brain homogenates were lysed in ice-cold lysis buffer (50 mM Tris–HCl pH = 7.5, 150 mM NaCl, 1% Triton X-100, 1 mM EDTA) supplemented with protease inhibitor cocktail (Roche, Indianapolis, IN). Supernatants were collected and protein concentrations determined using Bio-Rad Protein Assay Dye Reagent Concentrate (Hercules, CA). For each sample, the volume corresponding to 50 μg of protein was reduced with TCEP (Sigma-Aldrich, St Louis, MO) for 10 min and subsequently carbamidomethylated with iodoacetamide (Sigma-Aldrich, St Louis, MO) for 30 min in the dark. Protein digestion was performed using Sequencing Grade Modified Trypsin (Promega, Madison, WI) on S-Trap (ProtiFi, USA) microspin columns as elsewhere reported (103,104). Digested peptides were eluted from the S-Trap columns, vacuum dried and kept at −80°C until analysis.

Liquid chromatography–mass spectrometry/mass spectrometry and quantitative proteomic analysis

Peptide mixtures were suspended in 0.2% formic acid and 500 ng of each sample were loaded on an EASY-nLC II chromatographic system coupled with an LTQ-Orbitrap XL mass spectrometer (Thermo Scientific, Bremen, Germany). Liquid chromatography—tandem mass spectrometry (LC–MS/MS) analysis was performed as elsewhere reported (105–107). Proteome Discoverer™ version 1.4.1.14 (Thermo Scientific, Bremen, Germany) was employed for proteomic analysis, set as described (106). *Mus musculus* was selected as taxonomy. $Arx^{KO/Y}$, $Arx^{(GCG)7/Y}$ and XY WT proteomic datasets resulted constituted by about 1000 proteins identified by a minimum of two peptides (Supplementary Material, Tables S1 and S2). The normalized spectral abundance factor (NSAF) was calculated and used as abundance index for each protein in the global dataset (102,108). Protein relative abundance in $Arx^{KO/Y}$ and $Arx^{(GCG)7/Y}$ samples was calculated as ratio of the NSAFs (both with respect to WT samples), and finally expressed in the log2 scale, obtaining the $\log_2$ fold change (FC). In particular, the proteins characterized by a $FC > 0.4$ or < -0.4 (corresponding to 1.3 ratio) were included in final proteomic datasets as differentially expressed proteins (DEPs). Hierarchical clustering dendrogram using Euclidean distances were carried out. DEPs were further filtered retaining only statistically significant FCs, whereas the Student's *t*-test between the two analysed groups was ≤ 0.05 (107,109).

Computational analysis and gene ontology enrichment

The hierarchical clustering analysis and heatmap of the identified proteins were performed using the MetaboAnalyst 4.0 software (http://www.metaboanalyst.ca) (64,110); Data were log-transformed and Pareto-scaled. Normal distribution of NSAF values in $Arx^{KO/Y}$, $Arx^{(GCG)7/Y}$ and XY WT proteomes was verified (Supplementary Material, Fig. S9). To annotate molecular functions of DEPs, Gene ontology (GO) mapping and Kyoto encyclopaedia of genes and genomes (KEGG) pathways analysis were performed using DAVID gene ontology analysis (http://david.abcc. ncifcrf.gov/). Bioinformatic analysis of altered biological processes was carried out using Ingenuity pathway analysis (IPA; https://digitalinsights.

qiagen.com/). Protein–protein interaction (PPI) network analysis was obtained using STRING (Search Tool for the Retrieval of Interacting Genes/Proteins; https://string-db.org) online database (111). The highest confidence (>0.9) of the argument of interactions was set. Public microarray datasets (GSE12956) (20) were downloaded from G.E.O. repository using *ad hoc* modified GEO2R pipeline. For microarray expression the analysis was performed in R (version 3.6.1) using the following packages: Biobase (version 2.46.0), GEOquery (version 2.54.1), limma (version 3.42.2), gprofiler2 (version 0.1.9). Briefly, extracted data were normalized, divided in two groups ($Arx^{KO/Y}$ and XY WT mice at E14.5) and log2 transformed. Differential expression was measured using limma package. Multiple test correction was performed applying the false discovery rate (FDR) method. The FDR threshold to identify differentially expressed genes was set to ≤ 0.05. Heat maps reporting log2 transformed signal intensities and Z-scores (Supplementary Material, Fig. S1) were generated using custom scripts in R language using the following packages: heatmap.2 function in ggplot2 (version 3.3.2) and RColorBrewer (version 1.1.2). ARX-bound genes were retrieved from ChIP-on-chip data in Supplementary material of the paper from Quillé and colleagues (31). Gene/protein ID conversion were performed using the online tool g:Profiler and the Uniprot database (https://www.uniprot.org) where needed. Intersection between gene/protein lists were first performed in R and then the graphical output (Venn diagram) was generated using Venny online tool (https://bioinfogp.cnb.csic.es/tools/venny/index.html).

Primary cortical neurons, depolarization experiments and immunocytochemistry

Cortical neurons were prepared from $Arx^{(GCG)7/Y}$ and XY WT neonatal brains (3 mice *per* culture experiment). Cortices were dissected and dissociated to single cells suspension with 0.125% trypsin. Cells were maintained in Neurobasal medium (NB, Gibco, Carlsbad, CA), 1% B-27 plus supplement (Gibco, Carlsbad, CA), 10% Horse serum (Gibco, Carlsbad, CA), 2 mM L-glutamine and penicillin/streptomycin (Gibco, Carlsbad, CA). At DIV 4, cells were treated with 10 mM Cytosine arabinoside (Sigma-Aldrich, St Louis, MO) for 48 h. Membrane depolarization was induced at culture days *in vitro* 11 (DIV11) by addition of depolarization buffer with high potassium concentration (170 mM KCl, 2 mM $CaCl_2$, 1 mM $MgCl_2$, 10 mM Hepes) for 10 min. NaCl buffer solution was used as a control (112). After 24 h, cortical neurons were collected to perform expression transcript analysis. Quantitative PCR was performed with SYBR-Green-based reagents (Bio-Rad, Hercules, CA) using a CFX96 real-time PCR Detection system (Bio-Rad, Hercules, CA) to evaluate *c-fos* transcript abundance (Supplementary Material, Table S9).

For immunocytochemistry, primary cortical neurons were cultured on coverslips. At DIV10 were fixed with 4% paraformaldehyde (PFA, Gibco, Carlsbad, CA) in phosphate saline buffer (PBS) (Gibco, Carlsbad, CA), permeabilized in PBS with 0.03% Triton-X and blocked in PBS/bovine serum albumin (BSA) 3%. The following primary antibodies were used: mouse anti-β III tubulin (dilution 1:750, T8578, Sigma-Aldrich, St Louis, MO); rabbit anti-Map2 (dilution 1:400, AB5622, Merck Millipore, Darmstadt, Germany); while as secondary antibodies we used: Texas Red antimouse (T862, 1:400, Life Technologies, Carlsbad, CA) and Alexa Fluor 488 antirabbit (dilution 1:400, A11034, Life Technologies, Carlsbad, CA). Nuclei were counterstained with DAPI (1 μg/mL, D1306, Life Technologies, Carlsbad, CA). Images were taken using a laser-scanning microscope (LSM 700, Carl Zeiss Microimaging, Inc.) equipped with a plan neofluor ×20 (NA 0.5) or plan neofluor ×40 oil immersion (NA 1.3) objective lens or diode lasers (at 405 and 555 nm) were used as light source. Z-slices from the top to the bottom of the cells were collected and 3D reconstructions were carried out using the LSM 700 software. Alternatively, images were acquired using a Nikon Eclipse inverted microscope equipped with Nikon DMS-Ri2 camera.

SUnSET assay

Culture days *in vitro* 7 (DIV7) of murine primary cortical neurons were incubated with puromycin (Sigma-Aldrich, St Louis, MO) for 30 min. Cells were washed with ice-cold PBS and lysed directly in RIPA buffer (Sigma-Aldrich, St Louis, MO). Samples were analysed by western blotting and puromycin incorporation was detected using the mouse monoclonal antibody MABE343 (dilution 1:10 000, 12D10 clone, Sigma-Aldrich, St Louis, MO). Coomassie staining of total proteins were done and immunolabelling of the housekeeping protein HSP90 was used as loading control.

RNA extraction and alternative splicing analysis

Total RNA extraction and DNAse treatment were performed according to the manufacturer's protocols (Life Technologies, Carlsbad, CA). Then, reverse transcription was performed with Superscript III Reverse Transcription kit (Life Technologies, Carlsbad, CA). Alternative splicing abundances were determined using the AmpliTaq DNA Polymerase (Applied Biosystems, Thermo Scientific, Bremen, Germany) on the Biorad PCR System (BioRad Laboratories Inc., Hercules, USA). *C. elegans* samples were similarly treated, except for the flash-freezing of worm pellets before proceeding with RNA extraction in TRI Reagent® (Merck, Darmstadt, Germany) and FastStart™ Taq DNA Polymerase (Roche, Basel, Switzerland) used for determination of alternative splicing abundance. The oligonucleotide sequences used in mice and *C. elegans* studies are reported in Supplementary Material, Table S9. For *Neurexin* analysis, alternative transcripts in mice were analysed by using oligonucleotides reported in Iijima et al. (54) whereas in *C. elegans* oligonucleotides were as reported in Kuroyanagi et al. (113). In mouse, the measures of transcript analysis were normalized to *Hprt* RNA level, while in *C. elegans* transcript analysis were

normalized to *act-1* RNA level. Each experiment assay was performed in triplicate in three independent experiments. DNA fragment intensities were quantified by using ImageJ software.

Immunoblotting and antibodies

Protein extraction in murine brain tissues and in *C. elegans* were prepared by standard methods described elsewhere (4,100). Membranes were blocked with 5% non-fat dry milk and the following antibodies were used: antitubulin (dilution 1:100 000, #t6074, Sigma-Aldrich, St Louis, MO), antiacetyl tubulin (dilution 1:100 000, #t7451, Sigma-Aldrich, St Louis, MO), anti-Puf60 (dilution 1:1000, ab22819, Abcam, Cambridge, UK) and anti-eiF4A2 (dilution 1:40 000, ab31218, Abcam, Cambridge, UK). As secondary antibodies, we used antimouse (dilution 1:10 000, sc-2005 Santa Cruz Biotechnology, Dallas, TX), antigoat (dilution 1:5000, sc-2020 Santa Cruz Biotechnology, Dallas, TX) and antirabbit (1:10 000, sc-2004 Santa Cruz Biotechnology, Dallas, TX). As loading controls anti-β-actin (dilution 1:5000, sc8432; Santa Cruz Biotechnology, Dallas, TX), anti-GAPDH/anti-Gpd2/3 (dilution 1:5000, ab181602, Abcam Cambridge, UK) and Hsp90 (dilution 1:50 000, E-AB-22072, Elabscience, Houston, TX) were used. The signals were detected with an enhanced chemiluminescence kit (Advansta, San Jose, CA). Films were processed for densitometry scanning using the ImageJ software.

Statistical analysis

One-way ANOVA with Dunn multiple comparisons test, Two-way ANOVA with Tukey's multiple comparisons test and Student's *t*-test were applied using the GraphPad Prism 7 software. *P*-values < 0.05 were considered significant.

Data Availability

The mass spectrometry proteomics data have been deposited to the ProteomeXchange Consortium (available at http://www.proteomexchange.org) *via* the Proteomics Identification database (PRIDE; http://ebi.ac.uk/pride) partner repository with the dataset identifier PXD021358.

Web Resources

DAVID, https://david.ncifcrf.gov/
GenBank, https://www.ncbi.nlm.nih.gov/genbank/
g:profiler, https://biit.cs.ut.ee/gprofiler/gost/
modENCODE, http://www.modencode.org/
IPA, https://digitalinsights.qiagen.com/
NCBI, https://www.ncbi.nlm.nih.gov/
OMIM, https://www.omim.org/
STRING, https://string-db.org
UCSC, https://genome.ucsc.edu/
Uniprot, https://www.uniprot.org/
Venny, https://bioinfogp.cnb.csic.es/tools/venny/index.html
Wormbase, https://wormbase.org/

Supplementary Material

Supplementary Material is available at *HMG* online.

Acknowledgements

We thank the RIKEN BioResource Center (BRC, Riken, Japan), IGB Mouse Facility, and IGB Integrated Microscopy Facility. We also thank P. Collombat for kindly providing the *Arx*-KO mouse colony, F. Cieri for technical assistance in *C. elegans* experiments, T. Cirillo for mouse colony maintenance and all members of the Miano Laboratory for critical discussions. For the *C. elegans alr-1* strains we would like to thank P. Sengupta (Brandeis University, Waltham, MA) and the GCG, which is funded by the NIH Office of Research Infrastructure Programs (P40 OD010440). We are grateful to D. Schlessinger (Baltimore, MD) for critical reading of this manuscript. We also are grateful to the SPECIALmente Noi Onlus Foundation for promoting research in autism spectrum disorder (ASD).

Funding

Telethon Foundation grant (Grant No. GGP14198) and Italian Ministry of Economic Development grant (Grant No. F/050011/02/X32) to M.G.M; Progetto di Ricerca di Rilevante Interesse Nazionale -PRIN (Grant No. 2017SNRXH3) to M.R.. D.D. received support from "Maria Rosaria Maglione Onlus Foundation".

Conflict of Interest statement. The authors declare that they have no conflicts of interest.

Authors' Contributions

D.D. and M.C. (Caterino) contributed to design of experiments, data analysis and writing the manuscript; L.V., M.C. (Costanzo), L.P., B.A., A.B., P.S. and S.P. contributed to performing experiments and data curation; G.T., E.D.S, M.R. contributed to interpretation of the results; M.B.L. contributed to the implementation of the research; V.C. contributed to data analysis and writing the manuscript; M.G.M. conceived the idea for the study, interpreted the results and wrote the manuscript with input from all the authors. All the authors have read and approved the final manuscript.

References

1. Wigle, J.T. and Eisenstat, D.D. (2008) Homeobox genes in vertebrate forebrain development and disease. *Clin. Genet.*, **73**, 212–226.
2. Laperuta, C., Spizzichino, L., D'Adamo, P., Monfregola, J., Maiorino, A., D'Eustacchio, A., Ventruto, V., Neri, G., D'Urso, M., Chiurazzi, P. *et al.* (2007) MRX87 family with Aristaless X dup24bp mutation and implication for polyalanine expansions. *BMC Med. Genet.*, **8**, 25.
3. Poeta, L., Fusco, F., Drongitis, D., Shoubridge, C., Manganelli, G., Filosa, S., Paciolla, M., Courtney, M., Collombat, P., Lioi, M. *et al.* (2013) A regulatory path associated with X-linked intellectual

disability and epilepsy links KDM5C to the polyalanine expansions in ARX. *Am. J. Hum. Genet.*, **92**, 114–125.
4. Poeta, L., Padula, A., Attianese, B., Valentino, M., Verrillo, L., Filosa, S., Shoubridge, C., Barra, A., Schwartz, C.E., Christensen, J. *et al.* (2019) Histone demethylase KDM5C is a SAHA-sensitive central hub at the crossroads of transcriptional axes involved in multiple neurodevelopmental disorders. *Hum. Mol. Genet.*, **28**, 4089–4102.
5. Bonneau, D., Toutain, A., Laquerriere, A., Marret, S., Saugier-Veber, P., Barthez, M.A., Radi, S., Biran-Mucignat, V., Rodriguez, D., Gélot, A. *et al.* (2002) X-linked lissencephaly with absent corpus callosum and ambiguous genitalia (XLAG): clinical, magnetic resonance imaging, and neuropathological findings. *Ann. Neurol.*, **51**, 340–349.
6. Okazaki, S., Ohsawa, M., Kuki, I., Kawawaki, H., Koriyama, T., Ri, S., Ichiba, H., Hai, E., Inoue, T., Nakamura, H. *et al.* (2008) Aristaless-related homeobox gene disruption leads to abnormal distribution of GABAergic interneurons in human neocortex: evidence based on a case of X-linked lissencephaly with abnormal genitalia (XLAG). *Acta Neuropathol.*, **116**, 453–462.
7. Olivetti, P.R. and Noebels, J.L. (2012) Interneuron, interrupted: molecular pathogenesis of ARX mutations and X-linked infantile spasms. *Curr. Opin. Neurobiol.*, **22**, 859–865.
8. Kato, M., Das, S., Petras, K., Kitamura, K., Morohashi, K., Abuelo, D.N., Barr, M., Bonneau, D., Brady, A.F., Carpenter, N.J. *et al.* (2004) Mutations of ARX are associated with striking pleiotropy and consistent genotype-phenotype correlation. *Hum. Mutat.*, **23**, 147–159.
9. Poeta, L., Drongitis, D., Verrillo, L. and Miano, M.G. (2020) DNA hypermethylation and unstable repeat diseases: a paradigm of transcriptional silencing to decipher the basis of pathogenic mechanisms. *Genes*, **11**, 684.
10. Shoubridge, C., Fullston, T. and Gécz, J. (2010) ARX spectrum disorders: making inroads into the molecular pathology. *Hum. Mutat.*, **31**, 889–900.
11. Mirzaa, G.M., Paciorkowski, A.R., Marsh, E.D., Berry-Kravis, E.M., Medne, L., Alkhateeb, A., Grix, A., Wirrell, E.C., Powell, B.R., Nickels, K.C. *et al.* (2013) CDKL5 and ARX mutations in males with early-onset epilepsy *Pediatr. Neurol.*, **48**, 367–377.
12. Mattiske, T., Lee, K., Gecz, J., Friocourt, G. and Shoubridge, C. (2016) Embryonic forebrain transcriptome of mice with polyalanine expansion mutations in the ARX homeobox gene. *Hum. Mol. Genet.*, **25**, 5433–5443.
13. Nasrallah, M.P., Cho, G., Simonet, J.C., Putt, M.E., Kitamura, K. and Golden, J.A. (2012) Differential effects of a polyalanine tract expansion in Arx on neural development and gene expression. *Hum. Mol. Genet.*, **21**, 1090–1098.
14. Lee, K., Mattiske, T., Kitamura, K., Gecz, J. and Shoubridge, C. (2014) Reduced polyalanine-expanded Arx mutant protein in developing mouse subpallium alters Lmo1 transcriptional regulation. *Hum. Mol. Genet.*, **23**, 1084–1094.
15. Nasrallah, I.M., Minarcik, J.C. and Golden, J.A. (2004) A polyalanine tract expansion in Arx forms intranuclear inclusions and results in increased cell death. *J. Cell Biol.*, **167**, 411–416.
16. Friocourt, G., Kanatani, S., Tabata, H., Yozu, M., Takahashi, T., Antypa, M., Raguénès, O., Chelly, J., Férec, C., Nakajima, K. *et al.* (2008) Cell-autonomous roles of ARX in cell proliferation and neuronal migration during corticogenesis. *J. Neurosci.*, **28**, 5794–5805.
17. Kitamura, K., Yanazawa, M., Sugiyama, N., Miura, H., Iizuka-Kogo, A., Kusaka, M., Omichi, K., Suzuki, R., Kato-Fukui, Y., Kamiirisa, K. *et al.* (2002) Mutation of ARX causes abnormal development of forebrain and testes in mice and X-linked lissencephaly with abnormal genitalia in humans. *Nat. Genet.*, **32**, 359–369.
18. Colombo, E., Collombat, P., Colasante, G., Bianchi, M., Long, J., Mansouri, A., Rubenstein, J.L. and Broccoli, V. (2007) Inactivation of Arx, the murine ortholog of the X-linked lissencephaly with ambiguous genitalia gene, leads to severe disorganization of the ventral telencephalon with impaired neuronal migration and differentiation. *J. Neurosci.*, **27**, 4786–4798.
19. Kitamura, K., Itou, Y., Yanazawa, M., Ohsawa, M., Suzuki-Migishima, R., Umeki, Y., Hohjoh, H., Yanagawa, Y., Shinba, T., Itoh, M., Nakamura, K. *et al.* (2009) Three human ARX mutations cause the lissencephaly-like and mental retardation with epilepsy-like pleiotropic phenotypes in mice. *Hum. Mol. Genet.*, **18**, 3708–3724.
20. Colasante, G., Simonet, J.C., Calogero, R., Crispi, S., Sessa, A., Cho, G., Golden, J.A. and Broccoli, V. (2015) ARX regulates cortical intermediate progenitor cell expansion and upper layer neuron formation through repression of Cdkn1c. *Cereb. Cortex*, **25**, 322–335.
21. Dubos, A., Meziane, H., Iacono, G., Curie, A., Riet, F., Martin, C., Loaëc, N., Birling, M.C., Selloum, M., Normand, E. *et al.* (2018) A new mouse model of ARX dup24 recapitulates the patients' behavioral and fine motor alterations. *Hum. Mol. Genet.*, **27**, 2138–2153.
22. Fulp, C.T., Cho, G., Marsh, E.D., Nasrallah, I.M., Labosky, P.A. and Golden, J.A. (2008) Identification of Arx transcriptional targets in the developing basal forebrain. *Hum. Mol. Genet.*, **17**, 3740–3760.
23. Lim, Y., Cho, I.T., Shi, X., Grinspan, J.B., Cho, G. and Golden, J.A. (2019) Arx expression suppresses ventralization of the developing dorsal forebrain. *Sci. Rep.*, **18**, 226.
24. Melkman, T. and Sengupta, P. (2005) Regulation of chemosensory and GABAergic motor neuron development by the *C. elegans* Aristaless/Arx homolog alr-1. *Development*, **132**, 1935–1949.
25. Veeraval, L., O'Leary, C.J. and Cooper, H.M. (2020) Adherens junctions: guardians of cortical development. *Front. Cell Dev. Biol.*, **8**, 6.
26. Colombo, E., Galli, R., Cossu, G., Gécz, J. and Broccoli, V. (2004) Mouse orthologue of ARX, a gene mutated in several X-linked forms of mental retardation and epilepsy, is a marker of adult neural stem cells and forebrain GABAergic neurons. *Dev. Dyn.*, **231**, 631–639.
27. Beguin, S., Crépel, V., Aniksztejn, L., Becq, H., Pelosi, B., Pallesi-Pocachard, E., Bouamrane, L., Pasqualetti, M., Kitamura, K., Cardoso, C. *et al.* (2013) An epilepsy-related ARX polyalanine expansion modifies glutamatergic neurons excitability and morphology without affecting GABAergic neurons development. *Cereb. Cortex*, **6**, 1484–1494.
28. Lee, K., Ireland, K., Bleeze, M. and Shoubridge, C. (2017) ARX polyalanine expansion mutations lead to migration impediment in the rostral cortex coupled with a developmental deficit of calbindin-positive cortical GABAergic interneurons. *Neuroscience*, **15**, 220–231.
29. Curie, A., Friocourt, G., des Portes, V., Roy, A., Nazir, T., Brun, A., Cheylus, A., Marcorelles, P., Retzepi, K., Maleki, N. *et al.* (2018) Basal ganglia involvement in ARX patients: the reason for ARX patients very specific grasping? *Neuroimage Clin.*, **19**, 454–465.
30. Romaniello, R., Arrigoni, F., Fry, A.E., Bassi, M.T., Rees, M.I., Borgatti, R., Pilz, D.T. and Cushion, T.D. (2018) Tubulin genes and malformations of cortical development. *Eur. J. Med. Genet.*, **61**, 744–754.
31. Abella, J.V., Galloni, C., Pernier, J., Barry, D.J., Kjær, S., Carlier, M.F. and Way, M. (2016) Isoform diversity in the Arp2/3 complex

determines actin filament dynamics. *Nat. Cell Biol.*, **18**, 76–86.
32. Lanzetti, L., Palamidessi, A., Areces, L., Scita, G. and Di Fiore, P.P. (2004) Rab5 is a signalling GTPase involved in actin remodelling by receptor tyrosine kinases. *Nature*, **429**, 309–314.
33. Lasser, M., Tiber, J. and Lowery, L.A. (2018) The role of the microtubule cytoskeleton in neurodevelopmental disorders. *Front. Cell. Neurosci.*, **12**, 165.
34. Kapur, M., Monaghan, C.E. and Ackerman, S.L. (2017) Regulation of mRNA translation in neurons-a matter of life and death. *Neuron*, **96**, 616–637.
35. Quillé, M.L., Carat, S., Quéméner-Redon, S., Hirchaud, E., Baron, D., Benech, C., Guihot, J., Placet, M., Mignen, O., Férec, C. *et al.* (2011) High-throughput analysis of promoter occupancy reveals new targets for Arx, a gene mutated in mental retardation and interneuronopathies. *PLoS One*, **6**, e25181.
36. Aiken, J., Buscaglia, G., Bates, E.A. and Moore, J.K. (2017) The α-tubulin gene *TUBA1A* in brain development: a key ingredient in the neuronal isotype blend. *J. Dev. Biol.*, **5**, 8.
37. Belvindrah, R., Natarajan, K., Shabajee, P., Bruel-Jungerman, E., Bernard, J., Goutierre, M., Moutkine, I., Jaglin, X.H., Savariradjane, M., Irinopoulou, T. *et al.* (2017) Mutation of the α-tubulin Tuba1a leads to straighter microtubules and perturbs neuronal migration. *J. Cell Biol.*, **216**, 2443–2461.
38. Kunwar, A.J., Rickmann, M., Backofen, B., Browski, S.M., Rosenbusch, J., Schöning, S., Fleischmann, T., Krieglstein, K. and Fischer von Mollard, G. (2011) Lack of the endosomal SNAREs vti1a and vti1b led to significant impairments in neuronal development. *Proc. Natl. Acad. Sci. U. S. A.*, **108**, 2575–2580.
39. Martinez, Y. and N'Gouemo, P. (2010) Blockade of the sodium calcium exchanger exhibits anticonvulsant activity in a pilocarpine model of acute seizures in rats. *Brain Res.*, **1366**, 211–216.
40. Pilo Boyl, P., Di Nardo, A., Mulle, C., Sassoè-Pognetto, M., Panzanelli, P., Mele, A., Kneussel, M., Costantini, V., Perlas, E., Massimi, M. *et al.* (2007) Profilin2 contributes to synaptic vesicle exocytosis, neuronal excitability, and novelty-seeking behavior. *EMBO J.*, **26**, 2991–3002.
41. Tokudome, K., Okumura, T., Shimizu, S., Mashimo, T., Takizawa, A., Serikawa, T., Terada, R., Ishihara, S., Kunisawa, N., Sasa, M. and Ohno, Y. (2016) Synaptic vesicle glycoprotein 2A (SV2A) regulates kindling epileptogenesis via GABAergic neurotransmission. *Sci. Rep.*, **6**, 27420.
42. Amorim, I.S., Lach, G. and Gkogkas, C.G. (2018) The role of the eukaryotic translation initiation factor 4E (eIF4E) in neuropsychiatric disorders. *Front. Genet.*, **9**, 561.
43. Costa, V., Sommese, L., Casamassimi, A., Colicchio, R., Angelini, C., Marchesano, V., Milone, L., Farzati, B., Giovane, A., Fiorito, C. *et al.* (2010) Impairment of circulating endothelial progenitors in down syndrome. *BMC Med. Genet.*, **3**, 40.
44. Kasem, E., Kurihara, T. and Tabuchi, K. (2018) Neurexins and neuropsychiatric disorders. *Neurosci. Res.*, **127**, 53–60.
45. Colasante, G., Sessa, A., Crispi, S., Calogero, R., Mansouri, A., Collombat, P. and Broccoli, V. (2009) Arx acts as a regional key selector gene in the ventral telencephalon mainly through its transcriptional repression activity. *Dev. Biol.*, **334**, 59–71.
46. Zheng, C., Diaz-Cuadros, M., Nguyen, K.C.Q., Hall, D.H. and Chalfie, M. (2017) Distinct effects of tubulin isotype mutations on neurite growth in *Caenorhabditis elegans Mol. Biol. Cell.*, **28**, 2786–2801.
47. Niu, W., Lu, Z.J., Zhong, M., Sarov, M., Murray, J.I., Brdlik, C.M., Janette, J., Chen, C., Alves, P., Preston, E. *et al.* (2011) Diverse transcription factor binding features revealed by genome-wide ChIP-seq in *C. elegans*. *Genome Res.*, **21**, 245–254.
48. Fukushige, T., Siddiqui, Z.K., Chou, M., Culotti, J.G., Gogonea, C.B., Siddiqui, S.S. and Hamelin, M. (1999) MEC-12, an alpha-tubulin required for touch sensitivity in *C. elegans*. *J. Cell Sci.*, **112**, 395–403.
49. Hurd, D.D., Miller, R.M., Núñez, L. and Portman, D.S. (2010) Specific alpha- and beta-tubulin isotypes optimize the functions of sensory cilia in *Caenorhabditis elegans*. *Genetics*, **185**, 883–896.
50. Green, K.M., Glineburg, M.R., Kearse, M.G., Flores, B.N., Linsalata, A.E., Fedak, S.J., Goldstrohm, A.C., Barmada, S.J. and Todd, P.K. (2017) RAN translation at C9orf72-associated repeat expansions is selectively enhanced by the integrated stress response. *Nat. Commun.*, **8**, 2005.
51. Poeta, L., Padula, A., Lioi, M.B., van Bokhoven, H. and Miano, M.G. (2021) Analysis of a set of KDM5C regulatory genes mutated in neurodevelopmental disorders identifies temporal coexpression brain signatures. *Genes*, **12**, 1088.
52. Thompson, M., Bixby, R., Dalton, R., Vandenburg, A., Calarco, J.A. and Norris, A.D. (2019) Splicing in a single neuron is coordinately controlled by RNA binding proteins and transcription factors. *elife*, **8**, e46726.
53. Geuens, T., Bouhy, D. and Timmerman, V. (2016) The hnRNP family: insights into their role in health and disease. *Hum. Genet.*, **135**, 851–867.
54. Iijima, T., Wu, K., Witte, H., Hanno-Iijima, Y., Glatter, T., Richard, S. and Scheiffele, P. (2011) SAM68 regulates neuronal activity-dependent alternative splicing of neurexin-1. *Cell*, **147**, 1601–1614.
55. Gomez, A.M., Traunmüller, L. and Scheiffele, P. (2021) Neurexins: molecular codes for shaping neuronal synapses. *Nat. Rev. Neurosci.*, **22**, 137–151.
56. Chih, B., Gollan, L. and Scheiffele, P. (2006) Alternative splicing controls selective trans-synaptic interactions of the neuroligin-neurexin complex. *Neuron*, **51**, 171–178.
57. Matsuda, K. and Yuzaki, M. (2011) Cbln family proteins promote synapse formation by regulating distinct neurexin signaling pathways in various brain regions. *Eur. J. Neurosci.*, **33**, 1447–1461.
58. Philbrook, A., Ramachandran, S., Lambert, C.M., Oliver, D., Florman, J., Alkema, M.J., Lemons, M. and Francis, M.M. (2018) Neurexin directs partner-specific synaptic connectivity in *C. elegans*. *elife*, **7**, e35692.
59. Calahorro, F. (2014) Conserved and divergent processing of neuroligin and neurexin genes: from the nematode C. elegans to human. *Invertebr. Neurosci.*, **14**, 79–90.
60. Haklai-Topper, L., Soutschek, J., Sabanay, H., Scheel, J., Hobert, O. and Peles, E. (2011) The neurexin superfamily of *Caenorhabditis elegans*. *Gene Expr. Patterns*, **11**, 144–150.
61. Buchsbaum, I.Y., Kielkowski, P., Giorgio, G., O'Neill, A.C., Di Giaimo, R., Kyrousi, C., Khattak, S., Sieber, S.A., Robertson, S.P. and Cappello, S. (2020) ECE2 regulates neurogenesis and neuronal migration during human cortical development. *EMBO Rep.*, **21**, e48204.
62. Hamada, N., Ogaya, S., Nakashima, M., Nishijo, T., Sugawara, Y., Iwamoto, I., Ito, H., Maki, Y., Shirai, K., Baba, S. *et al.* (2018) De novo PHACTR1 mutations in west syndrome and their pathophysiological effects. *Brain*, **141**, 3098–3114.
63. Muñoz-Lasso, D.C., Romá-Mateo, C., Pallardó, F.V. and Gonzalez-Cabo, P. (2020) Much more than a scaffold: cytoskeletal proteins in neurological disorders. *Cell*, **9**, 358.
64. Breuss, M.W., Leca, I., Gstrein, T., Hansen, A.H. and Keays, D.A. (2017) Tubulins and brain development - the origins of functional specification. *Mol. Cell. Neurosci.*, **84**, 58–67.

65. Creppe, C., Malinouskaya, L., Volvert, M.L., Gillard, M., Close, P., Malaise, O., Laguesse, S., Cornez, I., Rahmouni, S., Ormenese, S. *et al.* (2009) Elongator controls the migration and differentiation of cortical neurons through acetylation of alpha-tubulin. *Cell*, **136**, 551–564.
66. Poirier, K., Saillour, Y., Bahi-Buisson, N., Jaglin, X.H., Fallet-Bianco, C., Nabbout, R., Castelnau-Ptakhine, L., Roubertie, A., Attie-Bitach, T., Desguerre, I. *et al.* (2010) Mutations in the neuronal ß-tubulin subunit TUBB3 result in malformation of cortical development and neuronal migration defects. *Hum. Mol. Genet.*, **19**, 4462–4473.
67. Guerrini, R. and Parrini, E. (2009) Neuronal migration disorders. *Neurobiol. Dis.*, **38**, 154–166.
68. Meroceles, P., Laquerrière, A., Adde-Michelm, C., Marret, S., Saugier-Veber, P., Beldjord, C. and Friocourt, G. (2010) Evidence for tangential migration disturbances in human lissencephaly resulting from a defect in LIS1, DCX and ARX genes. *Acta Neuropathol.*, **120**, 503–515.
69. Friocourt, G., Marcorelles, P., Saugier-Veber, P., Quille, M.L., Marret, S. and Laquerrière, A. (2011) Role of cytoskeletal abnormalities in the neuropathology and pathophysiology of type I lissencephaly. *Acta Neuropathol.*, **121**, 149–170.
70. Borovac, J., Bosch, M. and Okamoto, K. (2018) Regulation of actin dynamics during structural plasticity of dendritic spines: signaling messengers and actin-binding proteins. *Mol. Cell. Neurosci.*, **91**, 122–130.
71. Stouffer, M.A., Golden, J.A. and Francis, F. (2016) Neuronal migration disorders: focus on the cytoskeleton and epilepsy. *Neurobiol. Dis.*, **92**, 18–45.
72. Friocourt, G. and Parnavelas, J.G. (2011) Identification of Arx targets unveils new candidates for controlling cortical interneuron migration and differentiation. *Front. Cell. Neurosci.*, **5**, 28.
73. Siehr, M.S., Massey, C.A. and Noebels, J.L. (2020) *Arx* expansion mutation perturbs cortical development by augmenting apoptosis without activating innate immunity in a mouse model of X-linked infantile spasms syndrome. *Dis. Model. Mech.*, **13**, dmm042515.
74. De Pasquale, V., Caterino, M., Costanzo, M., Fedele, R., Ruoppolo, M. and Pavone, L.M. (2020) Targeted metabolomic analysis of a mucopolysaccharidosis IIIB mouse model reveals an imbalance of branched-chain amino acid and fatty acid metabolism. *Int. J. Mol. Sci.*, **21**, 4211.
75. Bonini, S.A., Mastinu, A., Ferrari-Toninelli, G. and Memo, M. (2017) Potential role of microtubule stabilizing agents in neurodevelopmental disorders. *Int. J. Mol. Sci.*, **18**, 1627.
76. Neumann, B. and Hilliard, M.A. (2014) Loss of MEC-17 leads to microtubule instability and axonal degeneration. *Cell Rep.*, **6**, 93–103.
77. Wei, D., Gao, N., Li, L., Zhu, J.X., Diao, L., Huang, J., Han, Q.J., Wang, S., Xue, H., Wang, Q. *et al.* (2018) α-Tubulin acetylation restricts axon overbranching by dampening microtubule plus-end dynamics in neurons. *Cereb. Cortex*, **28**, 3332–3346.
78. Beaudoin, G.M., Lee, S.H., Singh, D., Yuan, Y., Ng, Y.G., Reichardt, L.F. and Arikkath, J. (2012) Culturing pyramidal neurons from the early postnatal mouse hippocampus and cortex. *Nat. Protoc.*, **7**, 1741–1754.
79. Cagnetta, R., Wong, H.H., Frese, C.K., Mallucci, G.R., Krijgsveld, J. and Holt, C.E. (2019) Noncanonical modulation of the eIF2 pathway controls an increase in local translation during neural wiring. *Mol. Cell*, **73**, 474–489.
80. Jousse, C., Oyadomari, S., Novoa, I., Lu, P., Zhang, Y., Harding, H.P. and Ron, D. (2003) Inhibition of a constitutive translation initiation factor 2alpha phosphatase, CReP, promotes survival of stressed cells. *J. Cell Biol.*, **163**, 767–775.
81. Moon, S.L., Sonenberg, N. and Parker, R. (2018) Neuronal regulation of eIF2α function in health and neurological disorders. *Trends Mol. Med.*, **24**, 575–589.
82. Sossin, W.S. and Costa-Mattioli, M. (2019) Translational control in the brain in health and disease. *Cold Spring Harb. Perspect. Biol.*, **11**, a032912.
83. Zhu, P.J., Khatiwada, S., Cui, Y., Reineke, L.C., Dooling, S.W., Kim, J.J., Li, W., Walter, P. and Costa-Mattioli, M. (2019) Activation of the ISR mediates the behavioral and neurophysiological abnormalities in down syndrome. *Science*, **366**, 843–849.
84. Carnemolla, A., Fossale, E., Agostoni, E., Michelazzi, S., Calligaris, R., De Maso, L., Del Sal, G., MacDonald, M.E. and Persichetti, F. (2009) Rrs1 is involved in endoplasmic reticulum stress response in Huntington disease. *J. Biol. Chem.*, **27**, 18167–18173.
85. Cheng, W., Wang, S., Mestre, A.A., Fu, C., Makarem, A., Xian, F., Hayes, L.R., Lopez-Gonzalez, R., Drenner, K., Jiang, J. *et al.* (2018) C9ORF72 GGGGCC repeat-associated non-AUG translation is upregulated by stress through eIF2α phosphorylation. *Nat. Commun.*, **9**, 51.
86. Lombardo, M.V., Moon, H.M., Su, J., Palmer, T.D., Courchesne, E. and Pramparo, T. (2018) Maternal immune activation dysregulation of the fetal brain transcriptome and relevance to the pathophysiology of autism spectrum disorder. *Mol. Psychiatry*, **23**, 1001–1013.
87. Scheper, G.C., Proud, C.G. and van der Knaap, M.S. (2006) Defective translation initiation causes vanishing of cerebral white matter. *Trends Mol. Med.*, **12**, 159–166.
88. Tordera, R.M., Garcia-García, A.L., Elizalde, N., Segura, V., Aso, E., Venzala, E., Ramírez, M.J. and Del Rio, J. (2011) Chronic stress and impaired glutamate function elicit a depressive-like phenotype and common changes in gene expression in the mouse frontal cortex. *Eur. Neuropsychopharmacol.*, **21**, 23–32.
89. Low, K.J., Ansari, M., Abou Jamra, R., Clarke, A., El Chehadeh, S., FitzPatrick, D.R., Greenslade, M., Henderson, A., Hurst, J., Keller, K. *et al.* (2017) PUF60 variants cause a syndrome of ID, short stature, microcephaly, coloboma, craniofacial, cardiac, renal and spinal features. *Eur. J. Hum. Genet.*, **25**, 552–559.
90. Rusconi, F., Paganini, L., Braida, D., Ponzoni, L., Toffolo, E., Maroli, A., Landsberger, N., Bedogni, F., Turco, E., Pattini, L. *et al.* (2015) LSD1 Neurospecific alternative splicing controls neuronal excitability in mouse models of epilepsy. *Cereb. Cortex*, **25**, 2729–2740.
91. Vuong, C., Black, D. and Zheng, S. (2016) The neurogenetics of alternative splicing. *Nat. Rev. Neurosci.*, **17**, 265–281.
92. Weyn-Vanhentenryck, S.M., Feng, H., Ustianenko, D., Duffié, R., Yan, Q., Jacko, M., Martinez, J.C., Goodwin, M., Zhang, X., Hengst, U. *et al.* (2018) Precise temporal regulation of alternative splicing during neural development. *Nat. Commun.*, **9**, 2189.
93. Castronovo, P., Baccarin, M., Ricciardello, A., Picinelli, C., Tomaiuolo, P., Cucinotta, F., Frittoli, M., Lintas, C., Sacco, R. and Persico, A.M. (2020) Phenotypic spectrum of NRXN1 mono- and bi-allelic deficiency: a systematic review. *Clin. Genet.*, **97**, 125–137.
94. Danilenko, M., Dalgliesh, C., Pagliarini, V., Naro, C., Ehrmann, I. and Feracci, M. (2017) Binding site density enables paralog-specific activity of SLM2 and Sam68 proteins in Neurexin2 AS4 splicing control. *Nucleic Acids Res.*, **45**, 4120–4130.
95. Bryant, C.D. and Yazdani, N. (2016) RNA-binding proteins, neural development and the addictions. *Genes Brain Behav.*, **15**, 169–186.

96. Low, Y.H., Asi, Y., Foti, S.C. and Lashley, T. (2021) Heterogeneous nuclear ribonucleoproteins: implications in neurological diseases. *Mol. Neurobiol.*, **58**, 631–646.
97. Poirier, K., Van Eschm, H., Friocourt, G., Saillour, Y., Bahi, N., Backer, S., Souil, E., Castelnau-Ptakhine, L., Beldjord, C., Francis, F. *et al.* (2004) Neuroanatomical distribution of ARX in brain and its localisation in GABAergic neurons. *Brain Res. Mol. Brain Res.*, **122**, 35–46.
98. Marchese, E., Valentini, M., Di Sante, G., Cesari, E., Adinolfi, A., Corvino, V., Ria, F., Sette, C. and Geloso, M.C. (2021) Alternative splicing of neurexins 1-3 is modulated by neuroinflammation in the prefrontal cortex of a murine model of multiple sclerosis. *Exp. Neurol.*, **335**, 113497.
99. Collombat, P., Mansouri, A., Hecksher-Sorensen, J., Serup, P., Krull, J., Gradwohl, G. and Gruss, P. (2003) Opposing actions of Arx and Pax4 in endocrine pancreas development. *Genes Dev.*, **17**, 2591–2603.
100. Verrillo, L., Mangano, E., Drongitis, D., Merelli, I., Pischedda, F., Piccoli, G., Consolandi, C., Bordoni, R. and Miano, M.G. (2020) A reliable strategy for single-cell RNA sequencing analysis using cryoconserved primary cortical cells. *J. Neurosci. Methods*, **347**.
101. Brenner, S. (1974) The genetics of *Caenorhabditis elegans*. *Genetics*, **77**, 71–94.
102. De Pasquale, V., Costanzo, M., Siciliano, R.A., Mazzeo, M.F., Pistorio, V., Bianchi, L., Marchese, E., Ruoppolo, M., Pavone, L.M. and Caterino, M. (2020) Proteomic analysis of mucopolysaccharidosis IIIB mouse brain. *Biomol. Ther.*, **10**, 355.
103. Caterino, M., Ruoppolo, M., Orrù, S., Savoia, M., Perrotta, S., Del Vecchio, L., Salvatore, F., Stewart, G.W. and Iolascon, A. (2006) Characterization of red cell membrane proteins as a function of red cell density: annexin VII in different forms of hereditary spherocytosis. *FEBS Lett.*, **580**, 6527–6532.
104. Costanzo, M., Caterino, M., Cevenini, A., Jung, V., Chhuon, C., Lipecka, J., Fedele, R., Guerrera, I.C. and Ruoppolo, M. (2020) Proteomics reveals that methylmalonyl-CoA mutase modulates cell architecture and increases susceptibility to stress. *Int. J. Mol. Sci.*, **21**, 4998.
105. Caterino, M., Corbo, C., Imperlini, E., Armiraglio, M., Pavesi, E., Aspesi, A., Loreni, F., Dianzani, I. and Ruoppolo, M. (2013) Differential proteomic analysis in human cells subjected to ribosomal stress. *Proteomics*, **13**, 1220–1227.
106. Costanzo, M., Cevenini, A., Marchese, E., Imperlini, E., Raia, M., Del Vecchio, L., Caterino, M. and Ruoppolo, M. (2018) Label-free quantitative proteomics in a methylmalonyl-CoA mutase-silenced neuroblastoma cell line. *Int. J. Mol. Sci.*, **19**, 3580.
107. Imperlini, E., Spaziani, S., Mancini, A., Caterino, M., Buono, P. and Orrù, S. (2015) Synergistic effect of DHT and IGF-1 hyperstimulation in human peripheral blood lymphocytes. *Proteomics*, **15**, 1813–1818.
108. Caterino, M., Zacchia, M., Costanzo, M., Bruno, G., Arcaniolo, D., Trepiccione, F., Siciliano, R.A., Mazzeo, M.F., Ruoppolo, M. and Capasso, G. (2018) Urine proteomics revealed a significant correlation between urine-fibronectin abundance and estimated-GFR decline in patients with Bardet-Biedl syndrome. *Kidney Blood Press. Res.*, **43**, 389–405.
109. Capobianco, V., Caterino, M., Iaffaldano, L., Nardelli, C., Sirico, A., Del Vecchio, L., Martinelli, P., Pastore, L., Pucci, P. and Sacchetti, L. (2016) Proteome analysis of human amniotic mesenchymal stem cells (hA-MSCs) reveals impaired antioxidant ability, cytoskeleton and metabolic functionality in maternal obesity. *Sci. Rep.*, **6**, 25270.
110. Costanzo, M., Fiocchetti, M., Ascenzi, P., Marino, M., Caterino, M. and Ruoppolo, M. (2021) Proteomic and Bioinformatic investigation of altered pathways in neuroglobin-deficient breast cancer cells. *Molecules*, **26**, 2397.
111. Caterino, M., Ruoppolo, M., Mandola, A., Costanzo, M., Orrù, S. and Imperlini, E. (2017) Protein-protein interaction networks as a new perspective to evaluate distinct functional roles of voltage-dependent anion channel isoforms. *Mol. BioSyst.*, **13**, 2466–2476.
112. Ding, X., Liu, S., Tian, M., Zhang, W., Zhu, T., Li, D., Deng, H., Jia, Y., Xie, W., Xie, H. *et al.* (2017) Activity-induced histone modifications govern Neurexin-1 mRNA splicing and memory preservation. *Nat. Neurosci.*, **20**, 690–699.
113. Kuroyanagi, H., Watanabe, Y., Suzuki, Y. and Hagiwara, M. (2013) Position-dependent and neuron-specific splicing regulation by the CELF family RNA-binding protein UNC-75 in *Caenorhabditis elegans*. *Nucleic Acids Res.*, **41**, 4015–4025.